Title:

A change from warm/humid to cold/dry climate conditions recorded in lower Barremian clay-dominated continental successions from the SE Iberian Chain (NE Spain).

Authors:

Elisa Laita (*)

Blanca Bauluz

Marcos Aurell

Beatriz Bádenas

José Ignacio Canudo

Alfonso Yuste

IUCA-Department of Earth Sciences, Faculty of Sciences, Universidad de Zaragoza, Pedro Cerbuna 12, 50009-Zaragoza, Spain.

(*) corresponding author: laita@unizar.es IUCA-Department of Earth Sciences, Faculty of Sciences, Universidad de Zaragoza, Pedro Cerbuna 12, 50009-Zaragoza, Spain.

Abstract

A combined facies and clay mineralogy analysis of the continental succession recorded in the lower part of the Blesa Formation (early Barremian, Oliete subbasin, NE Spain) allowed us to specify the palaeoclimatic and palaeoenvironmental conditions under which this sedimentary record originated. Six outcrops including clays, clays/marls and dm-thick interbedded palustrine-lacustrine limestone levels were logged and sampled

for X-ray diffraction and optical and electron microscopy analysis. The lower levels consist of red clays with abundant ferruginous pisoids (1–5 mm in size) and macropisoids (>5 mm), whereas the intermediate and upper levels are ochre and violet clays/marls with few or no pisoids. The pisoids normally consist of a nucleus and a cortex made up of several layers. Some pisoids have a fragment of a previous pisoid acting as a nucleus, indicating local re-working processes. Both the nucleus and the cortex are formed by hematite, goethite, variable contents of kaolinite, and minor proportions of ilmenite. Their texture and mineralogy show an *in-situ* growth. Interbedded limestone beds within the clay- and clay/marl-dominated levels are formed by micrite, microsparite and sparite. These limestones are cemented by kaolinite and they also have pisoids, indicating the occurrence of edaphic processes. The red clays have the lowest calcite content and the highest hematite, anatase, diaspore, goethite and kaolinite content. By contrast, the ochre and violet clays/marls have higher illite content. Smectite is only detected in the ochre clays/marls. This mineral association is characteristic of lateritic palaeosols, formed under warm and humid conditions. Kaolinite and smectite textures indicate that they are authigenic, whereas illite may be of detrital origin. The upward decrease in kaolinite, hematite, anatase, diaspore and goethite content, along with the increase in quartz content and the presence of smectite and illite, reflect a change from warm and humid conditions to drier and colder conditions during the early Barremian in the studied area.

Keywords: palaeosols; palaeoclimate; pisoids; kaolinite; weathering

1. Introduction

The study of both facies and clay mineralogy in sedimentary successions is of great interest in allowing palaeoclimatic and palaeoenvironmental conditions to be inferred (Chamley, 1989; Velde, 1995; Thiry, 2000). In Mesozoic and Cenozoic sequences of continental materials, which include palaeosol developments, the variations in clay mineral assemblages have been widely used as palaeoclimatic and palaeoenvironmental proxies (e.g. Ehrmann et al. 2005; Raucskik and Varga, 2008; Do Campo et al. 2010; Bauluz et al. 2014, Do Campo et al. 2018 and references therein). Notably, palaeosols are formed in direct contact with the atmosphere, and thus clay minerals formed during their development can be correlated with climatic and palaeoenvironmental factors such as temperature, water availability during pedogenesis and vegetation cover, which control chemical weathering (Sheldon and Tabor, 2009; Varela et al. 2018).

Physical weathering processes predominate in dry and cold climates, and palaeosols that form under these conditions contain mineral assemblages dominated by illite and/or chlorite (Chamley, 1989). In contrast, intense hydrolysis processes take place under humid subtropical to tropical climates, giving rise to the formation of laterites, lateritic clays, and bauxites, where kaolinite is the main clay mineral (Chamley, 1989; Righi and Meunier, 1995). On the other hand, chemical weathering is less intense under warm climates with alternating humid and dry seasons, and in these cases smectite is formed (Buurman et al. 1988; Güven, 1988; Chamley, 1989; Murakami et al. 1996).

In NW Europe, a warm and humid climate was recorded during the early Barremian (Wright et al. 2000), which is also evidenced by the presence of ferruginous palaeosols and bauxites (Bárdossy, 1982). By contrast, an alternation of wet and dry seasons has been described during this period in the west of Europe (Haywood et al. 2004).

In the Iberian Range (NE Spain), a seasonal subtropical climate has been described during the Lower Cretaceous (Buscalioni and Fregenal-Martínez, 2010). Previous researchers pointed out the presence of Barremian kaolinite-rich clays, bauxite deposits and lateritic clays in this area (Combes, 1969; Molina and Salas, 1993; Bauluz et al. 2014, Yuste et al. 2015; Yuste et al. 2017), which is also consistent with relatively warm and humid conditions.

The link of clay mineral assemblages with the palaeoclimate-palaeoenvironment is not always straightforward. Clay-rich rocks and palaeosols frequently include not only authigenic clay minerals, but also others that formed during diagenetic processes. These processes could transform the clay minerals initially formed and therefore alter the palaeoclimatic-palaeoenvironmental signal (Dera et al. 2009; Bauluz et al. 2014). For this reason, it is necessary to conduct textural studies to assess possible diagenetic modifications in clay minerals before using them as palaeoclimatic indicators.

In this work, the use of X-ray diffraction and optical and electron microscopy to undertake a sedimentological, mineralogical and textural characterization of clay-rich outcrops present in the early Barremian (Lower Cretaceous) continental successions of the Oliete subbasin (Maestrazgo Basin; NE Spain) allowed us: 1) to characterize

sedimentary (*in-situ* vs. detrital) and diagenetic minerals; 2) to establish the variation in *in-situ* clay mineral assemblages and the palaeoenvironmental conditions under which they were formed; 3) to link the vertical trends of *in-situ* clay mineral assemblages with variations in the formation conditions, in particular temperature/humidity.

2. Geological Setting

The opening of the Atlantic Ocean along with the westward spread of the Tethys Ocean during the Late Jurassic-Early Cretaceous generated rifting processes in the eastern part of the Iberian Plate. During this active rifting period, extensional fault activity resulted in the progressive structural compartmentalization of the wide marine carbonate platforms that had previously developed during the Jurassic. All this resulted in the generation of independent subsiding rift-related sedimentary basins and subbasins, such as the Maestrazgo Basin in the eastern part of the Iberian Plate (e.g., Van Wees et al. 1998; Salas et al. 2001; Aurell et al. 2019).

The subbasin under study, the Oliete subbasin, is located in the northwestern marginal area of the Maestrazgo Basin (Fig. 1). The lower syn-rift sedimentary unit of the Oliete subbasin is the Blesa Formation, which reaches a thickness of up to 150 m (Canérot et al. 1982). This formation is divided into three genetic stratigraphic sequences: the lower Blesa (LBS), middle Blesa (MBS) and upper Blesa (UBS) sequences (Aurell et al. 2018). These authors describe the LBS as consisting of distal alluvial to palustrine marls/clays and palustrine-lacustrine limestones upwards and including clay-rich materials in its lowermost part; these are the materials studied in

the present work. The MBS is formed by oyster-rich limestones and marls grading upwards and landwards to distal alluvial and palustrine-lacustrine marls/clays and limestones. Finally, the UBS contains distal alluvial red clays in its lowermost part and palustrine and lacustrine carbonates and marls/clays towards the top (Aurell et al. 2018). The Barremian age of the Blesa Formation is well-constrained by the presence of charophytes in the palustrine–lacustrine marly and limestone facies found in the LBS and UPS (Canudo et al. 2010; Moreno-Azanza et al. 2014).

The lower part of the LBS studied here contains red to ochre and violet-ochre marls/clays of very variable thickness (0–60 m thick) at subbasin scale and local intercalations of carbonate-rich beds with root traces, charophytes and vertebrate fossils (Aurell et al. 2018 and references therein). Of particular interest for this work is the presence of dominant red clays in the lowermost part of the LBS, including ferruginous pisoids, thus indicating soil development at the onset of the sedimentation of the Blesa Formation. The tectono-sedimentary evolution at this initial development stage of the Oliete subbasin has been documented in Aurell et al. (2018). According to these authors, there was a period of subaerial exposure and erosion after the Jurassic marine carbonate sedimentation, which encompassed most of the Tithonian–Hauterivian, and normal faulting involved the overall tilting of the Jurassic limestones, which resulted in higher uplift and erosion of the areas located to the SW. In these areas only the lowermost Jurassic units are preserved from erosion (see the Montalbán Anticline in Fig. 2A), whereas a more complete Upper Jurassic succession is preserved in the NE domains (see the Alacón area in Fig. 2A). The angular erosive unconformity (Fig. 2C–E) over the tilted Jurassic limestones is linked

to a palaeokarst surface, which includes dissolution–precipitation meteoric features. The clay/marl-dominated succession of the lower part of the LBS studied here covers this palaeokarst (Fig. 2C, E). The main areas of clay-rich deposits with ferruginous pisoids within the Oliete subbasin are located in the northern (around Alacón) and southern regions (between the villages of Josa and Estercuel) (Fig. 2A). Further tectonic reactivation during the early Barremian gave rise to the development of an orthogonal system of NW–SE and NE–SW trending normal faults (Fig. 2B), which enabled the spreading of the distal alluvial and palustrine-shallow lacustrine sedimentation that characterizes most of the LBS (Aurell et al. 2018).

3. Methods

3.1. Logging and sampling

Six outcrops of the lower part of the LBS in the northern and southern areas of the Oliete subbasin were selected for logging and sampling (Fig. 2A). Logs ALC1, ALC2, ALC3 and VE are located to the north of the locality of Alacón, whereas logs JO and EST are found to the south of the towns of Josa and Estercuel, respectively.

The logged sections include different levels of red clays with pisoids, ochre or violet clays/marls with few or no pisoids, and a few intercalated palustrine-lacustrine limestone beds. Thickness, lithology, colour, texture and stratification were studied bed-by-bed, and a total of 47 samples of clays and clays/marls, palustrine-lacustrine limestones and ferruginous pisoids were taken for further analyses of texture and mineralogical composition in the laboratory (Table 1).

3.2. X-ray diffraction

The mineralogical composition of 47 samples was determined by X-ray diffraction (XRD). The <2 μm fractions of clay and clay/marl samples (n=33) were also analysed (Table 1). These fractions were concentrated by centrifugation and analysed on both air-dried and ethylene-glycol-treated oriented aggregates, following the procedure described by Bauluz et al. (2014). The diffraction patterns were obtained using a Philips 1710 diffractometer at the University of Zaragoza (Zaragoza, Spain), with 40 kV voltage, 30 mA current, CuKα radiation, automatic slit, and a graphite monochromator. The XRD patterns were acquired from 3 to 60º 2θ and 3 to 30º 2θ for whole samples and <2 μm fractions, respectively. The analyses were performed using the XPowderX software (Martin, 2017).

After determining the mineralogy of the samples, relative proportions of the mineral phases were acquired using Reference Intensity Ratio (RIR) values from Schultz (1964), Biscaye (1965) and Smith and Johnson (2000). The RIR values were calculated according to Hillier (2003). In addition, the full width at half maximum (FWHM) of the 001 reflections of kaolinite in both air-dried and ethylene-glycol-treated oriented aggregates was measured in order to determine kaolinite crystallinity.

3.3. Optical and Electron microscopy

Twenty-one thin sections of clays and clays/marls, palustrine-lacustrine limestones and ferruginous pisoids (coated with a thin layer of epoxy resin) were studied by both transmitted and reflected light microscopy in order to identify transparent and opaque minerals as well as to characterize their texture (Table 1). The description of the ferruginous particles was made following the terms given by Bárdossy (1982):

macropisoids (>5 mm), pisoids (1–5 mm), ooids (100 mm–1000 µm) and micro-ooids (<100 µm).

Seventeen thin sections were studied using a Carl Zeiss Merlin field emission scanning electron microscope (FESEM) equipped with an Oxford energy-dispersive X-ray (EDS) detector at the University of Zaragoza (Zaragoza, Spain) (Table 1). For this, the thin sections were previously carbon-coated. Compositional images of the samples were obtained using two types of backscattered electron detectors: angular selective (AsB) and energy selective (EsB). The accelerating voltage used for the former and for the EDS was 15 kV with a beam current of 400 pA. For the latter, the accelerating voltage was 4 kV with a beam current of 2.0 nA. In addition, morphological images were obtained from fragments of the rocks using a secondary electron detector (In-lens). In this case, the accelerating voltage was 5 kV with a beam current of 800 pA.

Semi-quantitative analyses were carried out using the EDS detector, which has a detection limit of 0.1%. From these analyses, clay mineral formulas were calculated in order to compare them with the theoretical compositions. The kaolinite formula was calculated on the basis of $O_5(OH)_4$, and the smectite and illite-type-phase formulas were calculated on the basis of $O_{10}(OH)_2$.

4. Results

4.1. Stratigraphy and facies distribution

4.1.1. Northern area

In the Alacón area (logs ALC1, ALC2, ALC3 and VE), the lower part of the LBS has a very variable thickness ranging from 3 to 23 m (Fig. 3A–C). Within individual logs there is a vertical distribution of facies from red clays with variable pisoid content to

ochre clays/marls with few pisoids, and to violet clays/marls without pisoids. In addition, a dm- to m-thick fibrous-radial nodular calcite bed and limestone beds are also recognized in the lower part of the successions, intercalated in the red clays.

Log correlation indicates that the number and thickness of clayey and limestone levels vary among the outcrops studied around Alacón (Fig. 3A). The first deposits of the LBS overlying the palaeokarstified Jurassic limestones correspond to a lowermost, 3-m-thick red clay level with fibrous-radial calcite nodules (5–12 cm in diameter) and pisoids, which is only recorded in log ALC2. This level pinches out laterally due to the irregular topography of the underlying palaeokarstified Jurassic limestones. A lower nodular limestone level (0.5 to 2 m thick) with fibrous-radial calcite nodules (5–10 cm in diameter) and some ferruginous pisoids overlies the basal red clay level in ALC2 and the palaeokarstic surface in ALC1, ALC3 and VE.

Upwards, red clay levels with abundant pisoids and intercalated palustrine-lacustrine limestone beds are recognized (Fig. 3A-D). Log correlation indicates variation in the number and thickness of red clay levels. In particular, there are three red clay levels (~1.5 m thick) in logs ALC1 and VE (levels 1 to 3 in Fig 3A), whereas there is only one level (up to 5 m thick) in log ALC3. The intercalated limestone beds are 0.6 to 2 m in thickness and contain ferruginous pisoids but no fibrous-radial calcite nodules.

Overlying the red clays with interbedded limestones, there is an ochre clay/marl level (4 to 5 m thick) that contains few ferruginous pisoids (level 4 in Fig. 3A), which in turn is overlain by a topmost 1.5 to 2 m-thick violet clay/marl level without pisoids (level 5 in Fig. 3A).

4.1.2. Southern area

The overall thickness of the lower part of the LBS is variable in the southern outcrops logged near Josa (JO, 9 m thick; Fig. 4A) and Estercuel (EST, 36 m thick; Fig. 4B). Successive red clay levels (3 to 6 m thick) overlie the palaeokarstic surface that developed over the Jurassic limestones. These levels contain abundant ferruginous pisoids (with the exception of the last level of red clays of EST). Limestone beds intercalated in these red clays are very scarce. In the EST log, a 0.3-m-thick limestone bed with fibrous-radial calcite nodules and pisoids, similar to that observed in ALC2 and VE, is interbedded between the two red clay levels with abundant pisoids. In the JO log, on top of the red clay there is a 0.3-m-thick palustrine-lacustrine limestone bed with micrite intraclasts and pisoids, but without fibrous-radial calcite nodules.

The successions end with an ochre clay/marl level (2 m thick in JO, 10 m thick in EST) and a 10-m-thick violet clay/marl level in the EST log. Neither the ochre nor the violet levels contain ferruginous pisoids.

4.2. Optical microscopy results

The fine-grained matrix of red clays and ochre and violet clays/marls are formed by clay minerals and oxides that cannot be identified at the resolution of the optical microscope. Occasionally, quartz fragments (10–600 μm) and micron-sized oxides can be recognized (Fig. 5A). Carbonate is observed as micritic nodules (Fig. 5B) or as sparitic crystals cementing the matrix (Fig. 5C). Microsparite carbonate cement is also observed in some samples.

The ferruginous pisoids found in the red clays and ochre clays/marls encompass macropisoids, pisoids and ooids/micro-ooids, following the classification proposed by Bárdossy (1982).

Macropisoids are spherical to ellipsoidal and have a nucleus formed by pisoids (Fig. 6A), ooids and micro-ooids coated by goethite and hematite with botryoidal textures (Fig. 6B, C, D and E), sometimes forming a sequence of alternate layers (25 to 700 µm thick) of both phases (Fig. 6B, D and E). Occasionally, an up to 1–3 mm-thick outer cortex formed by several concentric layers is observed over the nucleus of some macropisoids (Fig. 6D). The concentric layers consist of goethite, as deduced by optical properties under reflected light. Occasional quartz fragments and small rutile crystals are included among the cortex layers.

The pisoids display spherical and occasionally ellipsoidal morphologies. Using the classification of Guerrak (1987), they can be categorized as simple or fragmented. Simple pisoids show a massive nucleus and a cortex with several concentric layers (Fig. 5D), both formed by a mixture of iron oxides and clay minerals with occasional quartz fragments and rutile crystals. Fragmented pisoids have a nucleus formed by a fragment of a pisoid and a cortex with concentric layers similar to that of the simple pisoids (Fig. 5D). Some pisoids (both simple and fragmented) are fractured and partly replaced by sparitic carbonate (Fig. 5C). Broken pisoids are also observed. In addition, scour-and-fill textures, similar to those described by Taylor et al. (2008), are found in the cortex in some pisoids (Fig. 5E).

Ooids and micro-ooids (sensu Bárdossy, 1982) are also observed in some clayey levels. The size ranges from 200 to 400 µm for the ooids and from 20 to 100 µm for the micro-ooids. Like the simple pisoids, they present spherical morphologies with a massive nucleus and a cortex with concentric layers and are formed by hematite and goethite (Fig. 5F).

The palustrine-lacustrine limestones are formed mainly by micrite, locally with microsparite and sparite crystals, and they also contain some micritic nodules and intraclasts (1–4 mm in size; Fig. 5H), spherical ferruginous pisoids (1–4 mm) and ferruginous ooids (200–400 μm). Fe-rich pisoids are simple, with a massive nucleus and concentric layers; most of them are fractured and others are partly replaced by micritic and sparitic carbonate (Fig. 5G). Some limestones also contain fossil remains such as disarticulated bivalve shells (Fig. 5H).

4.3. XRD results

XRD patterns of samples of the clays and clays/marls of the ALC1 and EST logs are shown in Figure 7. The same mineral phases were detected in the samples taken in the rest of the outcrops. The XRD results show that the clays and clays/marls are formed mainly by calcite, quartz, and clay minerals, with minor quantities of orthoclase, hematite, goethite, anatase, rutile, ilmenite and diaspore. In the <2 μm fraction, abundant kaolinite with illite, smectite and mixed-layers of illite/smectite (I/S) and chlorite/smectite (C/S) are identified as clay minerals.

The red clays have the lowest calcite content but they present the highest hematite, anatase, diaspore, goethite and kaolinite content. By contrast, the ochre and violet clays/marls have higher illite content, and smectite is only detected in the ochre clays/marls.

Using the classification of Allix et al. (2011), the studied samples of clays and clays/marls show hybrid compositions including argillaceous mudstones, argillaceous marlstones, siliceous marlstones and calcareous mudstones. These variations in lithology are a consequence of the variable proportions of carbonates and silicates.

Specifically, the red clays correspond to argillaceous mudstones and argillaceous marlstones, whereas the ochre and violet clays/marls are formed by siliceous marlstones and calcareous mudstones. Palustrine-lacustrine limestones are classified as calcareous mudstones.

The relative proportions of mineral phases in the thickest outcrops (the ALC1, VE, JO and EST logs) are shown in Figure 8. Calcite detected by XRD is not represented, because, as will be explained below, a large part of it did not form coetaneously with the clays and clays/marls. Proportions of mineral phases vary from base to top. Quartz content increases upwards whereas hematite, goethite, anatase, rutile, ilmenite and diaspore content decrease. Furthermore, kaolinite is the only clay mineral in the lower red clays reaching more than 50%. Its content decreases upwards coeval with an increase in the variety of clay minerals, where illite, smectite and mixed-layers of I/S and C/S are detected along with the kaolinite. This change almost coincides with the change from red clays to ochre clays/marls. Finally, in the violet clays/marls at the top, the dominant clay mineral is illite.

Table 2 shows kaolinite crystallinity values, which are in general greater than 0.4 and thus indicate low crystallinity. Overall, comparison of the values measured in air-dried and ethylene-glycol-treated samples shows that there are no significant differences, except in some cases where the difference between the two values could be indicative of the presence of expandable components such as smectite.

As far as macropisoids are concerned, XRD patterns show that they contain quartz, calcite, clay minerals (kaolinite, as deduced from the FESEM study), hematite, goethite, ferrihydrite and ilmenite. The relative proportions of these minerals in four

macropisoids from the first and second red clay levels in the ALC1 and VE logs are shown in Figure 9 as an example. In particular, macropisoids are mainly formed by Fe oxyhydroxides (hematite, goethite and ferrihydrite), kaolinite, and occasionally lower proportions of ilmenite. Calcite was not included, for the same reason as in the case of the clays and clays/marls.

4.4. FESEM results

4.4.1. Backscattered and secondary electron images

Backscattered and secondary electron images of clay and clay/marl samples (Fig. 10) show that the matrix of red clays is formed by kaolinite, hematite, goethite, anatase/rutile and ilmenite. Quartz fragments and orthoclase with anhedral morphologies are occasionally observed.

Kaolinite appears mainly as subhedral to euhedral nanometric plates, commonly showing pseudohexagonal outlines (Fig. 10A and B) and less frequently forming booklets (Fig. 10C and D). In the ochre and violet clays/marls, Fe and Ti oxides are less abundant or are even absent. In these cases, smectite (in the ochre samples) with flake morphologies and illite with wavy shapes (Fig. 10E and F) are observed.

Pisoids and macropisoids are mainly composed of hematite and goethite, with different proportions of kaolinite and minor proportions of ilmenite and calcite. Oxides in the nucleus are occasionally observed to be acicular whereas those in the cortex are anhedral (Fig. 11A). Kaolinite in the pisoids, in both the nucleus and the cortex, shows the same morphologies as those observed in the matrix, occurring with platy shapes and random orientation (Fig. 11B) or, alternatively, forming booklet aggregates (Fig. 11C). Booklets are also observed filling the internal cavities of the

pisoids. These booklets are larger in size compared with those found in the matrix of the clays and the clays/marls and the nucleus of the pisoids. They reach up to 1 µm in diameter and more than 2 µm of longitudinal development in the direction of the c crystallographic axis (Fig. 11D). On the other hand, the concentric layers of the cortex show different proportions of kaolinite and Fe oxides, allowing one layer to be distinguished from another. Fe oxides also appear among the matrix of the clays and clays/marls (Figs. 11B and C).

Carbonate intraclasts found in the violet and ochre clays and clays/marls are formed by sparite and/or microsparite, whose EDS analyses show homogeneous calcite compositions (Fig. 12A). Partly dissolved, reworked calcite fragments cemented by kaolinite from the matrix are observed in the ochre and violet clays and clays/marls (Fig. 12B). The palustrine-lacustrine limestones are also locally cemented by kaolinite (Fig. 12C). On the other hand, the replacement of some fractured pisoids and partially of the clay matrix by sparitic calcite (Fig. 12D) is better observed with the FESEM images than by optical microscopy.

4.4.2. EDS results

The results of the EDS analyses were used to calculate chemical formulas for the kaolinite, smectite and illite found in the matrix of the red clays, ochre clays/marls and violet clays/marls (Table 3).

Three compositional groups of kaolinite were established: 1) platy kaolinite, 2) booklets of kaolinite, and 3) booklets of kaolinite filling the cavities of pisoids. The formulas calculated for the first and the second groups show that these kaolinites present low proportions of Fe, whereas the third group does not contain Fe.

The calculated smectite compositions of the ochre clays/marls correspond to dioctahedral smectites, as deduced from the higher content of trivalent cations (Al and Fe) in the octahedral layer. Furthermore, the tetrahedral charge is higher than the octahedral charge, so they correspond to a beidellite-type smectite. The illite composition presents lower K and higher Al and Fe content than the theoretical.

5. Discussion

5.1. The matrix of the clays and clays/marls

The XRD results of the clays and clays/marls of the LBS indicate that, according to the compositional classification of Allix et al. (2011), the lower red clays correspond to argillaceous mudstones and argillaceous marlstones, whereas the overlying ochre and violet clay/marl levels are formed by siliceous marlstones and calcareous mudstones. The sedimentary evolution in the LBS from continental clayey facies to palustrine-lacustrine carbonate facies described by Aurell et al. (2018) may account for the lithological variation found in the studied materials.

The combination of XRD and optical and electron microscopy shows that the red clays and ochre and violet clays/marls are formed by calcite, quartz and clay minerals, with minor quantities of orthoclase, hematite, goethite, anatase, rutile, ilmenite and diaspore. The lower red clays present the highest hematite, anatase, diaspore, goethite and kaolinite content and do not contain smectite or illite. The intermediate ochre clays/marls contain smectite and have higher illite content compared to the red clays. The upper violet clays/marls present the highest illite content compared to

the red clays and the ochre clays/marls, and they also contain mixed-layers of I/S and C/S, but they do not contain smectite.

The textural study by means of electron microscopy provides key information for the interpretation of the origin of these clay minerals in clays and clays/marls: 1) In the case of the platy kaolinites and kaolinite booklets recorded, electron microscopy analyses suggest that they are authigenic. The platy kaolinites present pseudohexagonal morphologies that are incompatible with a detrital origin, since erosion and transport processes would have modified them. In the same way, the kaolinite booklets are also thought to have an *in-situ* origin because they are so delicate that they cannot resist any transport processes (Bauluz et al. 2014). The presence of Fe, albeit in low proportions, in the kaolinites (both platy and booklets) found in the matrix of the clays and clays/marls may be substituting the Al in the octahedral sheet of kaolinite, as occurs in similar materials (Mendelovici et al. 1979). The low kaolinite crystallinity is probably due to the presence of Fe in the structure, as is common in weathering processes (Mestdagh et al. 1980; Cantinolle et al. 1984; Yuste et al. 2015). Alternatively, given that the electron beam of the microscope has a larger diameter than the kaolinite particles, the analyses could be contaminated with nanometric Fe oxides.

2) As far as smectite is concerned, which is only recorded in the ochre clays/marls, its flake-type morphology and its presence as cement in the matrix of these clays/marls also suggest an *in-situ* origin. The chemical composition corresponds to dioctahedral, beidellite-type smectite. This type of smectite has previously been described in similar materials as a result of the weathering of dioctahedral micas (Singh and

Gilkes, 1991). Therefore, both kaolinite and smectite were probably formed as a consequence of edaphic processes, which involved the dissolution of previous aluminum silicate phases (feldspars, micas) and the crystallization of new ones (kaolinite and smectite).

3) Regarding illite, which is abundant in the ochre and violet clays/marls, especially in the latter, its formation is normally associated with diagenetic environments (Bauluz et al. 2000). A detrital origin is described for illite in materials similar to those studied in the present work (Franceschelli et al. 2003). The illite-type phases found in the ochre and violet clays/marls are probably of detrital origin, given that the genesis conditions of kaolinite in soils are not compatible with illite genesis. The anhedral morphologies of these phases would corroborate their detrital origin (Bauluz et al. 2014).

Hematite and goethite are present not only in the matrix of the clays and clays/marls, but also in the pisoids found in the red clays and ochre clays/marls (see 5.2 below). This suggests that the oxides and oxyhydroxides found in the matrix have an edaphic origin. By contrast, the quartz fragments and orthoclase would be of detrital origin. The low quartz and orthoclase content and their anhedral morphologies suggest that they are relicts of the original rocks and were probably partially dissolved during weathering.

5.2. Ferruginous pisoids in red clays and ochre clays/marls

In soils, the formation of *in-situ* pisoids is related to dissolution and re-precipitation processes, which are controlled by several factors, such as climatic variations, the chemistry of the groundwater and the difference in mobility of the chemical

components of the parent rock during chemical weathering (Valeton, 1972; Bhattacharyya and Kakimoto, 1982). According to Bárdossy (1982), the formation of these particles requires permanent groundwater saturation. The presence of scour-and-fill features like those described by Taylor et al. (2008) in some of the studied pisoids thus shows deformation in a semi-plastic state, indicating water saturation (Yuste et al. 2015).

The studied pisoids are hematite-goethite pisoids, also including clay minerals (kaolinite, as deduced by FESEM analysis). Previous investigations classified pisoids according to their hematite and kaolinite content (Szamatek et al. 1993; Sayed and Youssed, 1996). The pisoids studied here could thus be classified as hematitic-kaolinitic pisoids. In fact, the differences in the kaolinite and Fe oxide contents observed in the cortex of the studied pisoids allow the different concentric layers to be distinguished.

The presence in the pisoids and macropisoids of hematite, goethite and kaolinite, with textural features similar to those observed in the matrix, along with their concentric structure comprising a nucleus and a cortex, indicates that they were formed *in-situ* during the development of the soils. The sequences of goethite-hematite layers observed in macropisoids have previously been described in gossan development on metallic deposits (Velasco et al. 2013). According to these authors, the presence of this alternation of goethite and hematite layers reflects a change to less humid conditions.

The fact that the Fe oxides are cementing kaolinite in the pisoids suggests that these oxides form at a late stage in comparison with the kaolinite during the edaphic

processes. On the other hand, the EDS results for the booklets of kaolinite filling the cavities of pisoids indicate that these booklets do not contain Fe and are larger in size compared with those found in the matrix of the clays and clays/marls, a fact that may be due to recrystallization during very early diagenesis.

5.3. The palustrine-lacustrine limestones

According to the classification by Allix et al. (2011), the palustrine-lacustrine limestones intercalated in red clays with pisoids correspond to calcareous mudstones. A rise in water level probably led to a palustrine-lacustrine environment where carbonate muds precipitated, resulting in the formation of the calcareous mudstones. The reworked calcite fragments cemented by kaolinite in the ochre and violet clays and clays/marls may come from these calcareous mudstones.

These calcareous mudstones also contain pisoids, most of them broken, and ferruginous ooids, which may be reworked from the underlying red clays. The possible decrease in the water level may have enhanced the overprint of edaphic processes in the palustrine-lacustrine limestone (e.g. limestone with micritic nodules/intraclasts), favouring the reworking and fracturation of some of the pisoids. Other authors have described reworking processes as suggesting different episodes in the development of soils (Mücke et al. 1999). These calcareous mudstones are also cemented by kaolinite, suggesting that they also underwent edaphic processes during the decrease in the water level.

5.4. Nodular limestones and diagenesis of clays and clays/marls

During the early diagenesis, the matrix of the clays and clays/marls was cemented by microsparite and sparite. In addition, diagenesis may have also generated the micritic

nodules and sparitic-microsparitic intraclasts observed in the ochre and violet clays/marls. Sparitic cement also filled the gaps and replaced some fractured pisoids found in red clays and ochre clays/marls. Thus, calcite was eliminated from the quantification results, since much of it results from the diagenesis.

In the AlC2, VE and EST sections, the beds of fibrous-radial calcite nodules also overlie a lowermost red clay level with pisoids. According to Rossi and Cañaveras (1992), many of the calcites included in freshwater cements forming during diagenesis are fibrous, so the fibrous-radial calcite nodules could have also been formed in the early diagenesis. Given the presence of pisoids and their location in the lower part of the LSB, these nodule-bearing beds would correspond to palustrine-lacustrine limestones. They would have been affected by intense early diagenetic processes during an initial unstable stage with frequent hiatuses/erosional gaps after the long, Tithonian–Hauterivian period of subaerial exposure represented by the karstified surface on top of the Jurassic limestones.

As indicated above, the morphology of the kaolinite and smectite from the matrix of the clays and clays/marls suggests an *in-situ* origin. These early diagenetic processes would therefore not have modified the clay mineralogy of the facies significantly.

5.5. Palaeoweathering events deduced from clay mineral assemblages

The mineralogical association in the studied clays and clays/marls, the red, ochre and violet colours, along with the presence of ferruginous pisoids in the red clays and ochre clays/marls, allow them to be classified as palaeosols. According to Schellmann (1981), lateritic palaeosols are formed by mineral assemblages of goethite, hematite, aluminum hydroxides, kaolinite and quartz. Several authors (e.g. Foos, 1991; Mücke

et al. 1999; Giovannini et al. 2017; Faris et al. 2019) have reported these mineral phases as well as the presence of ferruginous pisoids in lateritic palaeosols. The mineral assemblages and the high content of ferruginous pisoids in the lower red clays thus allow them to be classified as lateritic palaeosols.

The combination of XRD and electron microscopy showed that kaolinite is the dominant clay mineral in these lateritic palaeosols. The presence of this mineral suggests a warm and humid climate, along with an intense chemical weathering (Chamley, 1989; Raucsik and Varga, 2008; Bauluz et al. 2014), which are characteristic conditions of tropical climates (Molina and Salas, 1993; Yuste et al. 2017).

The generation of red lateritic soils alternated (and was coeval) with the deposition of palustrine-lacustrine limestone with broken pisoids, reflecting a rapid rise (and probably subsequent falls) in water level, which could be related with variations in humidity, with local developments of palustrine-lacustrine areas. The afore-mentioned sequences of goethite-hematite layers in macropisoids might also be related to these conditions.

In the intermediate and upper ochre and violet clays/marls, the presence of smectite (beidellite; only present in ochre clays/marls), illite (highest content in violet clays/marls) and mixed-layers of I/S and C/S coincides with a decrease in and near-absence of kaolinite content. This trend can be interpreted in accordance with the weathering pattern proposed by Sheldon and Tabor (2009). These authors suggest trends in clay mineralogy that reflect weathering patterns changing from warm/humid to cold/dry conditions: kaolinite→smectite→vermiculite→chlorite and mixed-layer phyllosilicates→ illite and mica. In our studied case, the vertical trend is:

kaolinite (dominant in red clays) → kaolinite, smectite and illite (intermediate ochre clays/marls) → illite and mixed-layer I/S and C/S (violet clays/marls), suggesting a less intense chemical weathering due to a change from warm and humid to colder and drier conditions. The absence of pisoids in the violet clays/marls would support the idea of generally drier conditions, which would have prevented permanent groundwater saturation and therefore pisoid formation.

In the east of the Maestrazgo Basin, the Cantaperdius Formation (Salas, 1987), which is equivalent in age to the formation studied here (Barremian–Aptian), includes lacustrine and palustrine limestones and the development of soils and laterites like those described by Combes (1969). In addition, karst bauxite deposits, probably originating from lateritic materials laterally equivalent to the Cantaperdius Formation, have been reported in the nearby Morella subbasin (Molina and Salas, 1993; Yuste et al. 2015). Furthermore, Lower Cretaceous lateritic and bauxitic deposits have been described in the Cuenca Basin by Fregenal-Martínez et al. (2017). On the other hand, several authors have also reported the presence of laterites and bauxites in the Catalan Coastal Ranges and the Pyrenees (Combes, 1969; Ordóñez et al. 1990; Reinhardt et al. 2018; Seranne et al. 2019). According to Salas et al. (2004), the bauxites of the Catalan Coastal Ranges were probably formed from lower Barremian lateritic clays of the Cantaperdius Formation, whereas Seranne et al. (2019) dated the bauxite event of the Pyrenees to between early Albian and latest Albian. Nevertheless, the age of these deposits within the Barremian–Aptian interval cannot be precisely established. It is thus not possible to determine whether the

early Barremian palaeoclimatic evolution (i.e., from humid to dry conditions) documented here was regional or local in extent.

A change from warm to cooler climatic conditions during the Barremian–Aptian has been described in Europe (Pucéat et al. 2003; Steuber et al. 2005; Dinis et al. 2020), but there is no general agreement as regards the trend in humidity during the Early Cretaceous. A humid climate is described in the northwestern part of Europe during the early Barremian (Wright et al. 2000). The temperature models show warm and humid conditions for this period along the northern margin of the Tethys (Bodin et al. 2009; Price et al. 2011), as well as an increase in humidity during the mid-Barremian (= upper lower–lower upper Barremian) recorded at least at a European scale (Mutterlose et al. 2014). By contrast, an alternation of wet and dry seasons during the early Barremian (Haywood et al. 2004) and a trend to more arid and dry conditions towards the Albian–Cenomanian (Rodríguez-López et al. 2006) have also been reported.

The seasonal subtropical climate during the Lower Cretaceous in the Iberian Range described by Buscalioni and Fregenal-Martínez (2010) is supported by the presence of Barremian bauxitic and lateritic deposits (Molina and Salas, 1993; Bauluz et al. 2014, Yuste et al. 2015; Yuste et al. 2017). In addition, the Cretaceous ocean circulation models of Pucéat et al. (2005) and Hay (2008) substantiate the prevalence of wetter conditions in Iberia, which could be related to a warm and humid equatorial current in the Western Tethys (Dinis et al. 2020).

6. Conclusions

A combination of facies analysis and XRD and optical and electron microscopy studies has allowed us to characterize the mineralogical and textural changes found in the successive clay/carbonate levels found in the lower Blesa Formation (early Barremian, Oliete subbasin).

The lower part of the studied succession consists of red clay levels with abundant pisoids, recording the lowest calcite content but the highest content in hematite, anatase, diaspore, goethite and kaolinite. The intermediate ochre clay/marl levels contain smectite and illite and have few or no pisoids. The upper violet clay/marl levels contain illite and do not have pisoids.

The morphologies of the kaolinite crystals (platy and booklets) found in the lower red clay levels indicate that the kaolinite is authigenic. The smectite frequently recorded in the intermediate ochre clay/marl levels corresponds to a beidellite-type smectite, and the flake-type crystals forming the matrix of these levels also indicate an *in-situ* origin. The genesis of the illite-type phases is not compatible with the formation of kaolinite, so they might be of detrital origin.

Episodic rises in water level resulted in the formation of the palustrine-lacustrine limestone levels which are found interbedded within the clay-dominated succession. These levels may contain pisoids reworked from the underlying palaeosol levels and are cemented by kaolinite, indicating that they underwent edaphic processes during the episodic stages of decreased water level.

The mineralogical composition and structure of pisoids and macropisoids indicate an *in-situ* origin during lateritic soil formation. The decrease in the water level also favoured

the reworking of the materials, involving the fracturing of some of these pisoids, which may have eventually formed the nucleus of pisoids formed in earlier stages of soil development.

During the early diagenesis, both the matrix of the clays and clays/marls was cemented and the cavities of the pisoids were filled by microsparite and sparite cements. This diagenesis did not affect the morphology of kaolinite and smectite.

The mineralogy of the red clay levels, along with the presence of ferruginous pisoids, indicates that they are lateritic palaeosols. Kaolinite is the dominant clay mineral in the lower red clay levels, indicating humid and warm climatic conditions and an intense chemical weathering. This is consistent with the palaeoclimate conditions described for the early Barremian in the NE Iberian. The decrease in the kaolinite and the oxide and oxyhydroxide contents from the bottom to the top of the stratigraphic profiles, along with the increase in the quartz content and the presence of smectite and illite, indicates a change to a less intense chemical weathering. These variations reflect a change from warm and humid to generally colder and drier conditions in the studied area across the early Barremian.

Acknowledgments

This work was supported by the European Regional Development Fund and the Government of Aragon [Aragosaurus Group: Geological Resources and Palaeoenvironments, grant number E18_20R] and the Spanish Ministry of Science, Innovation and Universities [grant number RTI2018-093419-B-I00]. The authors would like to acknowledge the use of the Servicio General de Apoyo a la Investigación-SAI,

University of Zaragoza. They would also like to thank C. Gallego for her advice during the FESEM sessions. E. Laita received a grant by the Government of Aragon for the development of her PhD. The authors would also like to thank the reviewers Dr T. Bover-Arnal and Dr J. M. Molina, whose comments and suggestions helped to improve the manuscript.

References

Allix, P., Burnham, A., Fowler, T., Herron, M., Kleinberg, R., Symington, B., 2011. Coaxing oil from Shale. Oilfield Review 22(4), 4–15.

Aurell, M., Soria, A.R., Bádenas, B., Liesa, C.L., Canudo, J.I., Gasca, J.M., Moreno-Azanza, M., Medrano-Aguado, E., Mélendez, A., 2018. Barremian synrift sedimentation in the Oliete subbasin (Iberian Basin, Spain): palaeogeographical evolution and distribution of vertebrate remains. Journal of Iberian Geology 44, 285–308. https://doi.org/10.1007/s41513-018-0057-3

Aurell, M., Fregenal-Martínez, M., Bádenas, B., Muñoz-García, M. B., Élez, J., Meléndez, N., de Santisteban, C., 2019. Middle Jurassic–Early Cretaceous tectono-sedimentary evolution of the southwestern Iberian Basin (central Spain): Major palaeogeographical changes in the geotectonic framework of the Western Tethys. Earth-Science Reviews 199, 102983. https://doi.org/10.1016/j.earscirev.2019.102983

Bárdossy, G. (1982). Karst Bauxites. Elsevier. 441 pp.

Bauluz, B., Mayayo, M.J., Fernández-Nieto, C., González López, J.M., 2000. Geochemistry of Precambrian and Paleozoic siliciclastic rocks from the Iberian Range (NE Spain): implications for source-area weathering, sorting, provenance, and tectonic setting. Chemical Geology 168, 135–150. https://doi.org/10.1016/S0009-2541(00)00192-3

Bauluz, B., Yuste, A., Mayayo, M.J., Canudo, J.I., 2014. Early kaolinization of detrital Weald facies in the Galve Subbasin (Central Iberian Chain, north-east Spain) and its relationship to paleoclimate. Cretaceous Research 50, 214–227. https://doi.org/10.1016/j.cretres.2014.03.014

Bhattacharyya, D.P., Kakimoto, P.L., 1982. Origin of ferriferous ooids: a SEM study of ironstone ooids and bauxite pisoids. Journal of Sedimentary Petrology 52(3), 849–857.

Biscaye, P.E., 1965. Mineralogy and sedimentation of recent deep-sea clay in the Atlantic Ocean and adjacent seas and oceans. Geological Society of American Bulletin 76, 803–832.

Bodin, S., Fiet, N., Godet, A., Matera, V., Westermann, S., Clément, A., Janssen, N.M.M., Stille, P., Föllmi, K.B., 2009. Early Cretaceous (late Berriasian to early Aptian) palaeoceanographic change along the northwestern Tethyan margin (Vocontian Trough, southeastern France): $\delta^{13}C$, $\delta^{18}O$ and Sr-isotope belemnite and whole-rock records. Cretaceous Research 30, 1247–1262. https://doi.org/10.1016/j.cretres.2009.06.006

Buscalioni, A.D., Fregenal-Martínez, M.A., 2010. A holistic approach to the palaeoecology of Las Hoyas Konservat-Lagerstätte (La Huérguina Formation, Lower

Cretaceous, Iberian Ranges, Spain). Journal of Iberian Geology 36 (2), 297-326. doi:10.5209/rev_JIGE.2010.v36.n2.13

Buurman, E., Meijer, E.L., van Wijck, J.H., 1988. Weathering of chlorite and vermiculite in ultramafic rocks of Cabo Ortegal, northwestern Spain. Clays and Clays Minerals 36, 263–269.

Cantinolle, P., Didier, P., Meunier, J.D., Parron, C., Guendon, J.L., Bocquier, G., Nahon, D., 1984. Kaolinites ferrifères et oxyhydroxydes de fer et d'alumine dans les bauxites des Canonettes (S.E. de la France). Clay Minerals 19, 125–135.

Canudo, J.I., Gasca, J.M., Aurell, M., Badiola, A., Blain, H.A., Cruzado-Caballero, P., Gómez-Fernández, D., Moreno-Azanza, M., Parrilla, J., Rabal-Garcés, R., Ruiz-Omeñaca, J.I., 2010. La Cantalera: an exceptional window onto the vertebrate biodiversity of the Hauterivian-Barremian transition in the Iberian Peninsula. Journal of Iberian Geology 36(2), 205–224.

Canérot, J., Cugny, P., Pardo, G., Salas, R., Villena, J. 1982. Ibérica Central-Maestrazgo. In: García, A (Ed.), El Cretácico de España. Madrid: Univ. Complutense de Madrid, 273–344.

Chamley, H., 1989. Clay sedimentology. Springer-Verlag, Berlin. Heidelberg New York, 623 pp.

Combes, P.J., 1969. Recherches sur la genèse des bauxites dans le nord-est de l'Espagne le Languedoc et l'Ariége (France). Ph.D. Thesis, Montpellier, France, 375 p.Dera, G.,

Pellenard, P., Neige, P., Deconinck, J-F., 2009. Distribution of clay minerals in Early Jurassic Peritethyan seas: Palaeoclimatic significance inferred from multiproxy comparisons. Palaeogeography, Palaeoclimatology, Palaeoecology 271, 39–51. https://doi.org/10.1016/j.palaeo.2008.09.010

Dinis, P.A., Carvalho, J., Callapez, P.M., Mendes, M.M., Santos, V.F., Fernandes, P., 2020. Composition of Lower Cretaceous mudstones of the Algarve Basin and implications for Iberian paleoclimates. Cretaceous Research 110, 104404. https://doi.org/10.1016/j.cretres.2020.104404

Do Campo, M., del Papa, C., Nieto, F., Hongn, F., Petrinovic, I., 2010. Integrated analysis for constraining palaeoclimatic and volcanic influences on clay-mineral assemblages in orogenic basins (Palaeogene Andean foreland, Northwestern Argentina). Sedimentary Geology 228, 98–112. https://doi.org/10.1016/j.sedgeo.2010.04.002

Do Campo, M., Bauluz, B., del Papa, C., White, T., Yuste, A., Mayayo, M.J., 2018. Evidence of cyclic climatic changes recorded in clay mineral assemblages from a continental Paleocene-Eocene sequence, northwestern Argentina. Sedimentary Geology 368, 44–57. https://doi.org/10.1016/j.sedgeo.2018.03.007

Ehrmann, W., Setti, M., Marinoni, L., 2005. Clay minerals in Cenozoic sediments off Cape Roberts (McMurdo Sound, Antarctica) reveal palaeoclimatic history. Palaeogeography, Palaeoclimatology, Palaeoecology 229, 187–211. https://doi.org/10.1016/j.palaeo.2005.06.022

Faris, N., Ram, R., Tardio, J., Bhargava, S., Pownceby, M.I., 2019. Characterisation of a ferruginous rare earth beating lateritic ore and implications for rare earth mineral processing. Minerals Engineering 134, 23–36. https://doi.org/10.1016/j.mineng.2019.01.019

Foos, A.M., 1991. Aluminous lateritic soils, Eleuthera, Bahamas: a modern analog to carbonate paleosols. Journal of Sedimentary Petrology 61(3), 340–348.

Franceschelli, M., Puxeddu, M., Gattiglio, M., 2003. Geochemistry and origin of chloritoid schist from the Alpi Apuane, Italy: evidence of a prevailing lateritic signature. European Journal of Mineralogy 15, 575–588. https://doi.org/10.1127/0935-1221/2003/0015-0575

Fregenal-Martínez, M. A., Meléndez, N., Muñoz-García, B., Elez, J., de la Horra, R., 2017. The stratigraphic record of the Late Jurassic-Early Cretaceous rifting in the Alto Tajo-Serranía de Cuenca region (Iberian Ranges, Spain): Genetic and structural evidences for a revision and a new lithostratigraphic proposal. Revista de la Sociedad Geológica de España 30, 113–142.

Giovannini, A.L., Bastos Neto, A.C., Porto, C.G., Pereira, V.P., Takehara, L., Barbanson, L., Bastos, P.H.S., 2017. Mineralogy and geochemistry of laterites from the Morro dos Seis Lagos Nb (Ti, REE) deposit (Amazonas, Brazil). Ore Geology Reviews 88, 461–480. https://doi.org/10.1016/j.oregeorev.2017.05.008

Guerrak, S., 1987. Metallogenesis of cratonic oolitic ironstone deposits in the Bled el Mass, Azzel Mani, Ahnet and Mouydir basins, Central Sahara. Geologische Rundschau 76, 903–922. https://doi.org/10.1007/BF01821072

Güven, N., 1988. Smectites. In: Bailey, S.W. (Ed.), Hydrous Pyllosilicates. Mineralogical Society of America, Reviews in Mineralogy 19, 497–559.

Hay, W.W., 2008. Evolving ideas about the Cretaceous climate and ocean circulation. Cretaceous Research 29, 725–753. https://doi.org/10.1016/j.cretres.2008.05.025

Haywood, A.M., Valdes, P.J., Markwick, P.J., 2004. Cretaceous (Wealden) climates: a modelling prospective. Cretaceous Research 25, 303–331. https://doi.org/10.1016/j.cretres.2004.01.005

Hillier, S., 2003. Quantitative analysis of clay and other minerals in sandstones by X-ray powder diffraction (XRPD). International Association of Sedimentologists. Special Publications 34, 213–251.

Martin, J.D., 2017. A software package for powder x-ray diffraction analysis. Qualitative, quantitative and microtexture. 121pp.

Mendelovici, E., Yariv, S.H., Villalba, R., 1979. Iron-bearing kaolinite in venezuelan laterites: I. Infrared spectroscopy and chemical dissolution evidence. Clay Minerals 14, 323–331.

Mestdagh, M.M., Vielvoye, L., Herbillon, A.J., 1980. Iron in kaolinite: II. The relationships between kaolinite and iron content. Clay Minerals 15, 1–13. https://doi.org/10.1180/claymin.1980.015.1.01

Molina, J.M., Salas, R., 1993. Bauxitas kársticas del Cretácico inferior en Fuentespalda (provincia de Teruel): Estratigrafía, origen y paleogeografía. Cuadernos de Geología Ibérica 17, 207–230.

Moreno-Azanza, M., Canudo, J.I., Gasca, J.M., 2014. Spheroolithid eggshells in the Lower Cretaceous of Europe. Implications for eggshell evolution in ornithischian dinosaurs. Cretaceous Research 51, 75–87. https://doi.org/10.1016/j.cretres.2014.05.017

Mücke, A., Badejoko, A., Akande, S.O., 1999. Petrographic-microchemical studies and origin of the Agbaja Phanerozoic Ironstone Formation, Nupe Basin, Nigeria: a product of a ferruginized ooidal kaolin precursor not identical to the Minette-type. Mineralium Deposita 34, 284–296.

Murakami, T., Isobe, H., Sato, T., Ohnuki, T., 1996. Weathering of chlorite in a quartz-chlorite schist. Mineralogical and chemical changes. Clays and Clay Minerals 44, 244–256.

Mutterlose, J., Bodin, S., Fähnrich, L., 2014. Strontium-isotope stratigraphy of the Early Cretaceous (Valanginian-Barremian): Implications for Boreal–Tethys correlation and paleoclimate. Cretaceous Research 50, 252–263. https://doi.org/10.1016/j.cretres.2014.03.027

Ordóñez, S., Fort, R., Bustillo, M., 1990. Estudio de las tierras raras en las bauxitas kársticas del noreste de la península ibérica. Estudios Geológicos 46, 373–384.

Price, G.D., Fözy, I., Janssen, N.M.M., Pálfy, J., 2011. Late Valanginian-Barremian (Early Cretaceous) palaeotemperatures inferred from belemnite stable isotope and Mg/Ca ratios Bersek Quarry (Gerecse Mountains, Transdanubian Range, Hungary). Palaeogeography, Palaeoclimatology, Palaeoecology 305, 1–9. https://doi.org/10.1016/j.palaeo.2011.02.007

Pucéat. E., Lécuyer, C., Sheppard, S.M.F., Dromart, G., Reboulet, S., Grandjean, P., 2003. Thermal evolution of Cretaceous Tehtyan marine waters inferred from oxygen isotope composition of fish tooth enamels. Paleoceanography and Paleoclimatology 18 (2), 1–12. https://doi.org/10.1029/2002PA000823

Pucéat, E., Lecuyer, C., Reisber, L., 2005. Neodymium isotope evolution of NW Tethyan upper ocean waters throughout the Cretaceous. Earth and Planteary Science Letters 236, 705–720. https://doi.org/10.1016/j.epsl.2005.03.015

Raucskik, B., Varga, A., 2008. Climato-environmental controls on clay mineralogy of the Hettangian-Bajocian successions of the Mecsek Mountains, Hungary: An evidence for extreme continental weathering during the early Toarcian oceanic anoxic event. Palaeogeography, Palaeoclimatology, Palaeoecology 265, 1–13. https://doi.org/10.1016/j.palaeo.2008.02.004

Reinhardt, N., Proenza, J.A., Villanova-de-Benavent, C., Aiglsperger, T., Bover-Arnal, T., Torró, L., Salas, R., Dziggel, A., 2018. Geochemistry and Mineralogy of Rare Earth

Elements (REE) in Bauxitic Ores of the Catalan Coastal Range, NE Spain. Minerals 8(12), 562. https://doi.org/10.3390/min8120562

Righi, D., Meunier, A., 1995. Origin of clays by rock weathering and soil formation. In: Velde, B (Ed), Origin and Mineralogy of Clays: Clays and the Environment. Springer-Verlag, Heidelberg, pp. 43–161. https://doi.org/10.1007/978-3-662-12648-6_3

Rodríguez-López, J.P., de Boer, P.L., Meléndez, N., Soria, A.R., Pardo, G., 2006. Windblown desert sands in coeval shallow marine deposits: a key for the recognition of coastal ergs in the mid-Cretaceous Iberian Basin, Spain. Terra Nova 18, 314–320. https://doi.org/10.1111/j.1365-3121.2006.00695.x

Rossi, C., Cañaveras, J.C., 1999. Pseudospherulitic fibrous calcite in paleo-groundwater, unconformity-related diagenetic carbonates (Paleocene of the Ager basin and Miocene of the Madrid basin, Spain). Journal of Sedimentary Research 69, 224–238. https://doi.org/10.2110/jsr.69.224

Salas, R., 1987. El Malm y el Cretaci inferior entre el Massis de Garrafi la Serra d'Espada. Ph.D. Thesis, University of Barcelona, Spain, 345p.

Salas, R., Guimerà, J., Mas, R., Martín-Closas, C., Meléndez, A. y Alonso, A., 2001. Evolution of the Mesozoic central Iberian Rift System and its Cainozoic inversion (Iberian chain). Peri-Tethys Memoir 6, 145–185.

Salas, R., Vaquer, R., Travé, A., 2004. Bauxitas kársticas y arcillas lateríticas barremienses de la Cadena Ibérica oriental y la Cadena Costero Catalana: Relaciones genéticas y áreas de procedencia. Geo-Temas 6, 123–126.

Sayed, E., Youssef, A.A., 1996. Sedimentaological studies on the central Wadi Kalabsha kaolin deposits, Southwest of Aswan, Egypy. Journal of mineralogy, petrology and economic geology 91, 353–363.

Schellmann, W., 1981. Considerations on the definition and classification of laterites. Proceedings of the International Seminar on Lateritisation Processes, Trivandrum, India. A.A. Balkema, Rotterdam, pp. 1–10.

Schultz L.G., 1964. Quantitative interpretation of mineralogical composition from X-ray and chemical data for the Pierre shale. USGS Professional Paper 391-C, 1–131.

Sheldon, N.D., Tabor, N.J., 2009. Quantitative paleoenvironmental and paleoclimatic reconstruction using paleosols. Earth-Science Reviews 95, 1–52. https://doi.org/10.1016/j.earscirev.2009.03.004

Singh, B., Gilkes, R.J., 1991. A potassium-rich beidellite from a laterite pallid zone in western Australia. Clay Minerals 26, 233–244.

Smith, D.K., Johnson, G.G. Jr., 2000. Digitized database quantification, DDBQ, analysis of complex mixtures using fully digitized patterns. Advances in X-ray Analysis 42, 276–286.

Steuber, T., Rauch, M., Masse, J.P., Graaf, J., Malkoc, M., 2005. Low-latitude seasonality of Cretaceous temperatures in warm and cold episodes. Nature 437(27), 1341–1344. http://doi.org/10.1038/nature04096

Szamatek, K., Barczuk, A., Youssed, E.A.A., 1993. Genesis and mineralogy of lateritic kaolin at Aswan area (Sw Egypt). Archiwum Mineralogicze (Warsaw) 2, 81–97.

Taylor, G., Eggleton, R.A., Foster, L.D., Tilley, D.B. Le Gleuher, M., Morgan, C.M. 2008. Nature of the Weipa Bauxite deposit, northern Australia. Australian Journal of Earth Science 55, 45–70. https://doi.org/10.1080/08120090802438241

Thiry, M., 2000. Palaeoclimatic interpretation of clay minerals in marine deposits: an outlook from the continental origin. Earth-Science Reviews 49, 201–221. https://doi.org/10.1016/S0012-8252(99)00054-9

Valeton, J., 1972. Bauxites, Elsevier, Amsterdam, 226 pp.

Van Wees, J.D., Arche, A., Beijdorff, C.G., López-Gómez, J., 1998. Temporal and spatial variations in tectonic subsidence in the Iberian Basin (eastern Spain): inferences from automated forward modelling of high-resolution stratigraphy (Permian–Mesozoic). Tectonophysics 300, 285–310. https://doi.org/10.1016/S0040-1951(98)00244-3

Varela, A.N. Raigemborn, M.S., Richiano, S., White, T., Poiré, A.G., Lizzoli, S., 2018. Late Cretaceous paleosols as paleoclimate proxies of high-latitude Southern Hemisphere: Mata Amarilla Formation, Patagonia, Argentina. Sedimentary Geology 363, 83–95. https://doi.org/10.1016/j.sedgeo.2017.11.001

Velasco, F., Herrero, J.M., Suárez, S., Yusta, I., Alvaro, A., Tornos, F., 2013. Supergene features and evolution of gossans capping massive sulphide deposits in the Iberian Pyrite Belt. Ore Geology Reviews 53, 181–203. https://doi.org/10.1016/j.oregeorev.2013.01.008

Velde, B., 1995. Origin and Mineralogy of Clays. Clays and the Environment. Springer-Verlag, Berlin. Heidelberg New York, 334 pp.

Wright, V.P., Taylor, K.G., Beck, V.H., 2000. The paleohydrology of Lower Cretaceous seasonal wetlands, Isle of Wight, Southern England. Journal of Sedimentary Research 70, 619-632.

Yuste, A., Bauluz, B., Mayayo, M.J., 2015. Genesis and mineral transformations in Lower Cretaceous karst bauxites (NE Spain): climatic influence and superimposed processes. Geological Journal 50, 839–857. https://doi.org/10.1002/gj.2604

Yuste, A., Bauluz, B., Mayayo, M.J., 2017. Origin and geochemical evolution from ferrallitized Clays to karst bauxite: An example from the Lower Cretaceous of NE Spain. Ore Geology Reviews 84, 67–69. https://dx.doi.org/10.1016/j.oregeorev.2016.12.025

Figure captions

Fig. 1 (A) Simplified geological map of the NE Iberian Peninsula (B) Palaeogeographical reconstruction of the main Early Cretaceous sedimentation areas in NE Iberia, including the studied Oliete subbasin within the Maestrazgo Basin (from Aurell et al. 2018).

Fig. 2 (A) Palaeogeological map of the Oliete subbasin showing the age of the youngest marine units preserved below the unconformity between the Jurassic and the Barremian Blesa Formation (modified from Aurell et al. 2018). The areas where the lowermost Blesa Formation (i.e. lower Blesa Sequence: LBS) includes frequent clays with pisoids are indicated in orange. The six outcrops of the lower part of the LSB logged and sampled in the present work are located near the villages of Alacón, Josa and Estercuel (see white circles). (B) Palaeogeography of the Oliete subbasin during the sedimentation of the LBS (modified from Aurell et al. 2018). (C) Field view around the ALC2 log showing the upper Kimmeridgian (UK) shallow marine carbonates overlain by the clays and limestones of the LBS. (D) Close view near the ALC2 log showing the irregular palaeokarstic surface (yellow dashed line) that developed at the boundary between the UK and the LBS, and overlain by a nodular level (nl) formed by abundant fibrous-radial calcite nodules. (E) Field view of the lowermost part of the LBS at the ALC-3 log showing the red clays (rc) overlying the UK.

Fig. 3 (A) Stratigraphic correlation between the four stratigraphic logs from the Alacón area (their geographical coordinates are ALC1: N41º2’42.0’’ W0º42’47.6’’; ALC2: N41º2’29.1’’ W0º42’42.4’’; ALC3: N41º2’3.3’’ W0º42’10.9’’; and VE: N41º02’46.5’’ W0º42’07’’). The proposed correlation is based on the observation of lateral continuity at outcrop scale in continuous outcrops. (B, C) Field views around the VE and ALC1 logs, respectively, showing the upper Kimmeridgian (UK) shallow marine limestones, overlain successively by red clays (rc), ochre clays/marls (oc) and violet clays/marls (vc). (D) Detail of ferruginous pisoids and macropisoids (up to several mm in diameter) found in the red clays.

Fig. 4 (A) Field view of the Josa (JO) outcrop (at N40º55'20.64" W0º44'33.18") showing the Bajocian-Bathonian (BA) shallow marine limestones, overlain by the red LBS succession. The stratigraphic log shows the red and ochre clays/marls found in this area. (B) Field view of the Estercuel (EST) outcrop (at N40º50'22.58" W0º39'36.53") showing the lowermost red clays over the upper Bajocian-Bathonian limestones (BA). The stratigraphic log shows the red clays, and ochre and violet clay/marls dominant in this section.

Fig. 5: Transmitted and reflected light optical microscopy images of the samples. (A) Clays and clays/marls including occasional quartz grains and Fe oxides. (B) Micritic carbonate nodules in violet clays/marls. (C) Sparitic carbonate cementing the matrix and replacing the external concentric layers of pisoids in the red clays (see arrows). (D) Simple and fragmented pisoids in the red clays. (E) Scour-and-fill texture in the cortex of a simple pisoid. (F) Ferruginous pisoids and ooids in the red clays (see arrow). (G) Pisoid partly replaced by carbonate in the ochre marls/clays. (H) Micritic intraclasts and disarticulated bivalve shell in a palustrine-lacustrine limestone sample. Qtz=quartz, Cb=carbonate.

Fig. 6: Reflected light optical microscopy images of different parts of a macropisoid showing: (A) a pisoid in the nucleus of the macropisoid. (B, C, D and E), goethite and hematite with botryoidal textures and/or forming a sequence of alternate layers. (D) the external cortex formed by concentric layers. Hem=hematite, Ght=goethite, Cb=carbonate.

Fig. 7: XRD patterns obtained from clay and clay/marl samples in the ALC1 log (samples 1–9) and EST log (samples 1–7). Clays=clay minerals, Qtz=quartz, Cal=calcite, Ght=goethite, Dsp=diaspore, Ant=anatase, Or=orthoclase, Rt=rutile, Ilm=ilmenite, Hem=hematite.

Fig. 8: Variations in mineral content of clays and clays/marls in the ALC1, VE, JO and EST logs. The Jurassic marine carbonate rocks are represented either by the latest Kimmeridgian Higueruelas Formation (Hig. Fm) or by the Bajocian-Bathonian Chelva Formation.

Fig. 9: Relative proportions of mineral phases in macropisoids from the first and second red clay levels of the ALC1 and VE logs.

Fig. 10: FESEM images of samples of red clays, ochre clays/marls and violet clays/marls. (A) Matrix of the red clays. (B) Pseudohexagonal kaolinite crystals in red clays. (C) and (D) Kaolinite booklets in red clays. (E) Smectite with flake morphologies in ochre clays/marls. (F) Illite-type morphologies in violet clays/marls. Kln=kaolinite, FeOx=Fe oxides, Qtz=quartz, Sm=smectite and Ilt=illite.

Fig. 11: FESEM images of ferruginous pisoids showing: (A) Nucleus and cortex contact with acicular (in the nucleus) and anhedral (in the cortex) oxide crystals. (B) Platy kaolinites in the nucleus of pisoids together with abundant Fe oxides. (C) Kaolinite booklets in the nucleus of pisoids. (D) Kaolinite booklets filling cavities observed within some pisoids.

Fig. 12: FESEM images of carbonates in the study samples. (A) Calcite intraclast in the matrix of the ochre clays/marls. (B) Reworked calcite fragment with evidence of dissolution and cemented by kaolinite in the ochre clays/marls. (C) Palustrine-lacustrine limestone where kaolinite is cementing calcite. (D) Sparitic calcite replacing the matrix of clays and clays/marls and the concentric layers of the cortex of pisoids. Sm=smectite, Cal=calcite, Kln=kaolinite.

Table 1: Summary of sample analyses at the laboratory (n=number of samples/analyses).

Table 2: Kaolinite crystallinity values of the samples of clays and clays/marls from the different outcrops measured in air-dried (AD) and ethylene-glycol-treated (EG) samples. Am=argillaceous mudstone; Amr=argillaceous marlstone; Smr=siliceous marlstone; Cm=Calcareous marlstone.

Table 3: EDS analysis (Wt%) of phyllosilicates detected in clay and clay/marl samples (standard deviation in brackets).

Field samples (**n=47**)	**X-ray diffraction** (Mineralogical composition)		**Optical and electron microscopy** (Texture & mineral identification)	
	whole rock (**n=47**)	<2 µm fraction of clays & clays/marls (**n=33**)	Optical microscopy (**n=21**)	Electron microscopy-FESEM/EDS (**n=17**)
Red clays- **24**	**24**	**24**	**9**	**7**
Ocher clays/marls- **7**	**7**	**7**	**2**	**2**
Violet clays/marls- **2**	**2**	**2**	**1**	**1**
Ferruginous pisoids- **6**	**6**	**-**	**5**	**3**
Limestones- **8**	**8**	**-**	**4**	**4**
	- Relative proportions of the mineral phases - Kaolinite crystallinity		-Textures -Identification of opaque and transparent minerals	-Micro- and nanotextures -Chemical composition of the phases
	Derived data			

Alacón						Josa and Estercuel					
Log	Sample number	Sample description	Facies	KC		Log	Sample number	Sample description	Facies	KC	
				AD(001)	EG(001)					AD(001)	EG(001)
ALC1	1	Am	red clays	0.5	0.5	JO	1	Am	red clays	0.5	0.4
	2	Amr	red clays	0.7	0.4		2	Am	red clays	0.4	0.4
	4	Am	red clays	0.5	0.6		4	Amr	ocher clays/marls	0.4	0.4
	6	Smr	red clays	0.6	0.4		5	Amr	ocher clays/marls	0.3	0.4
	7	Smr	red clays	0.5	0.4	EST	1	Am	red clays	0.3	0.3
	8	Smr	ocher clays/marls	0.3	0.5		2	Amr	red clays	0.4	0.5
	9	Smr	ocher clays/marls	0.4	0.3		3	Amr	red clays	0.4	0.4
ALC2	2M	Am	red clays	0.6	0.5		4	Am	red clays	0.4	0.6
	2V	Am	red clays	0.5	0.6		5	Am	ocher clays/marls	0.5	0.6
	3	Am	red clays	0.6	0.6		6	Amr	ocher clays/marls	0.2	0.6
ALC3	1	Amr	red clays	0.5	0.5		7	Am	violet clays/marls	0.3	0.3
	2M	Am	red clays	0.6	0.6						
	2V	Am	red clays	0.6	0.6						
VE	1-B	Am	red clays	0.6	0.6						
	1	Am	red clays	0.6	0.7						
	1-T	Am	red clays	0.5	0.6						
	4	Am	red clays	0.4	0.4						
	6	Smr	red clays	0.5	0.5						
	7	Amr	red clays	0.5	0.5						
	8	Amr	red clays	0.5	0.4						
	9	Cm	ocher clays/marls	0.6	0.5						

	O	Na	Mg	Al	Si	K	Ca	Ti	Fe	Calculated composition
Platy kaolinite (n=37)	49.80 (3.16)	0.05 (0.15)	0.08 (0.16)	21.81 (1.40)	25.30 (1.28)	0.28 (0.29)	-	0.38 (0.77)	2.30 (1.56)	$Fe_{0.1}Al_{1.8}Si_2O_5(OH)_4$
Kaolinite Booklets in matrix (n=6)	56.68 (5.04)	-	-	19.81 (3.00)	21.82 (3.23)	0.03 (0.05)	-	0.17 (0.30)	1.48 (1.41)	$Fe_{0.3}Al_{1.7}Si_2O_5(OH)_4$
Kaolinite Booklets in pisoids cavities (n=3)	52.77 (2.47)	-	-	22.04 (1.41)	25.08 (1.54)	0.12 (0.20)	-	-	-	$Al_{1.9}Si_{2.1}O_5(OH)_4$
Illitic phases (n=4)	42.50 (7.60)	-	1.21 (0.26)	14.12 (2.44)	26.50 (5.09)	3.72 (1.39)	5.46 (5.00)	0.94 (1.53)	5.55 (2.23)	$(K_{0.5},H_3O)(Al_{1.2}Mg_{0.2}Fe_{0.4})(Si_{3.4}Al_{0.6})O_{10}(OH)_2,(H_2O))$
Smectite (n=17)	46.31 (12.52)	0.07 (0.29)	0.87 (0.58)	14.42 (3.90)	24.23 (6.55)	1.93 (1.36)	4.58 (4.14)	1.15 (2.83)	6.44 (6.12)	$(Ca_{0.1}K_{0.2})(Al_{1.5}Fe_{0.4}Ti_{0.1}Mg_{0.1})(Si_{3.1}AL_{0.9})O_{10}(OH)_2nH_2O$

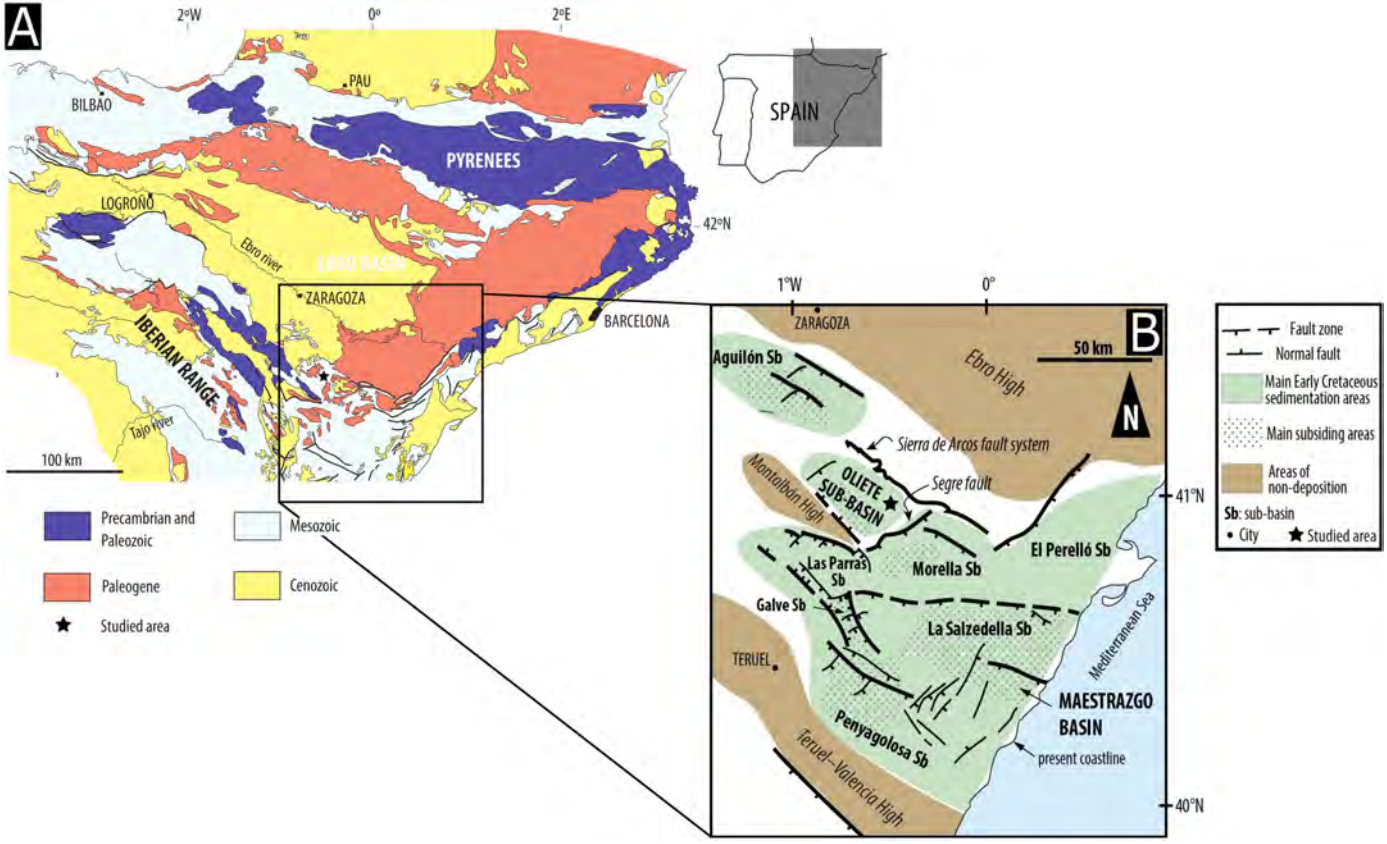
A
2°W
0°
2°E
BILBAO
PAU
PYRENEES
LOGROÑO
Ebro river
EBRO BASIN
42°N
ZARAGOZA
BARCELONA
IBERIAN RANGE
Tajo river
100 km
SPAIN
Precambrian and Paleozoic
Mesozoic
Paleogene
Cenozoic
Studied area
1°W
0°
ZARAGOZA
B
50 km
N
Aguilón Sb
Ebro High
Sierra de Arcos fault system
Montalbán High
OLIETE SUB-BASIN
Segre fault
41°N
El Perelló Sb
Las Parras Sb
Morella Sb
Galve Sb
La Salzedella Sb
Mediterranean Sea
TERUEL
MAESTRAZGO BASIN
Penyagolosa Sb
present coastline
Teruel–Valencia High
40°N
Fault zone
Normal fault
Main Early Cretaceous sedimentation areas
Main subsiding areas
Areas of non-deposition
Sb: sub-basin
City
Studied area

Figure 1

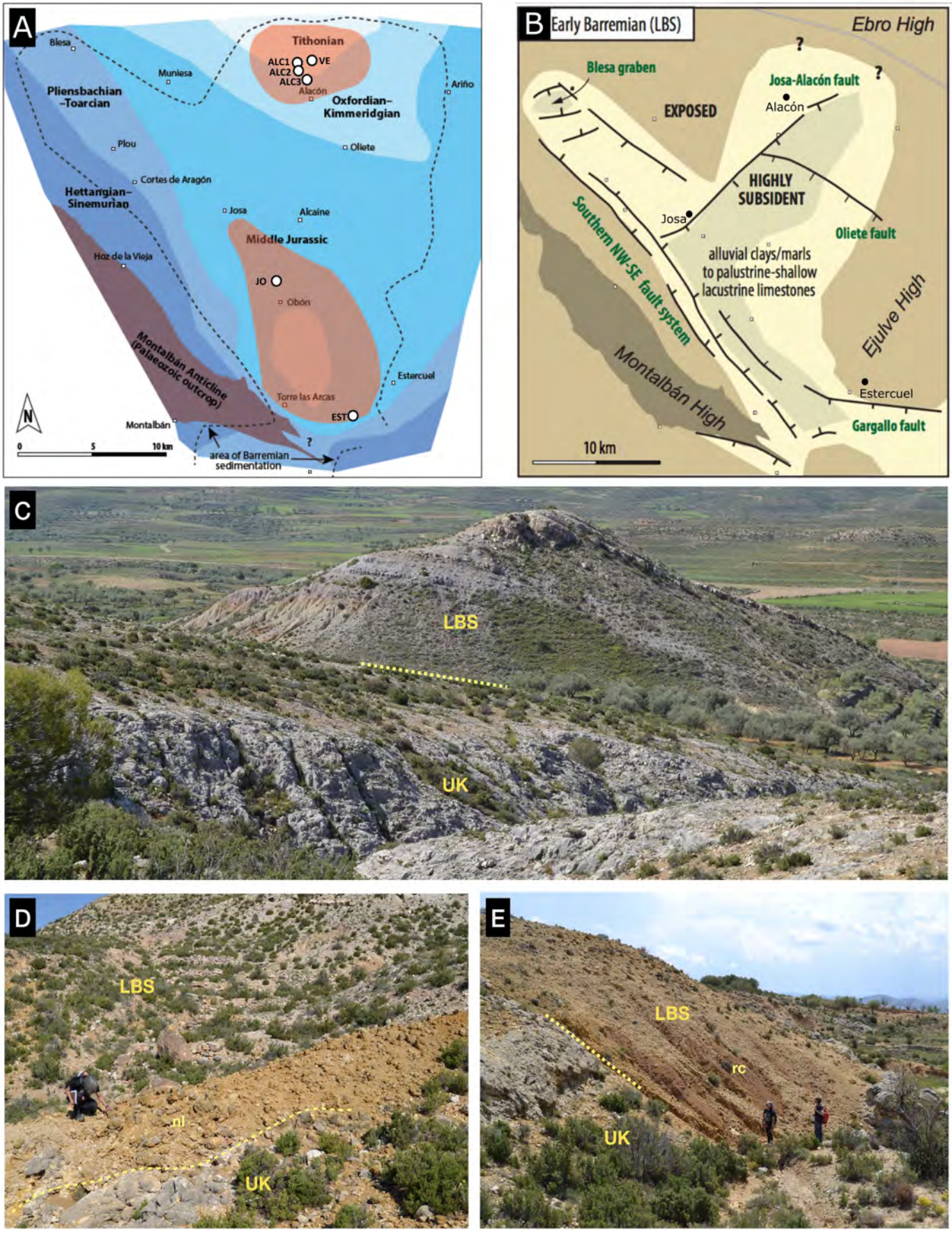
A
Blesa
Muniesa
Tithonian
ALC1
ALC2
ALC3
VE
Alacón
Ariño
Pliensbachian
–Toarcian
Oxfordian–
Kimmeridgian
Plou
Oliete
Cortes de Aragón
Hettangian–
Sinemurian
Josa
Alcaine
Middle Jurassic
Hoz de la Vieja
JO
Obón
Montalbán Anticline
(Palaeozoic outcrop)
Estercuel
Torre las Arcas
EST
N
Montalbán
0
5
10 km
?
area of Barremian
sedimentation
B
Early Barremian (LBS)
Ebro High
?
Blesa graben
Josa-Alacón fault
?
EXPOSED
Alacón
HIGHLY
SUBSIDENT
Josa
Oliete fault
Southern NW-SE fault system
alluvial clays/marls
to palustrine-shallow
lacustrine limestones
Ejulve High
Montalbán High
Estercuel
Gargallo fault
10 km
C
LBS
UK
D
LBS
nl
UK
E
LBS
rc
UK

Figure 2

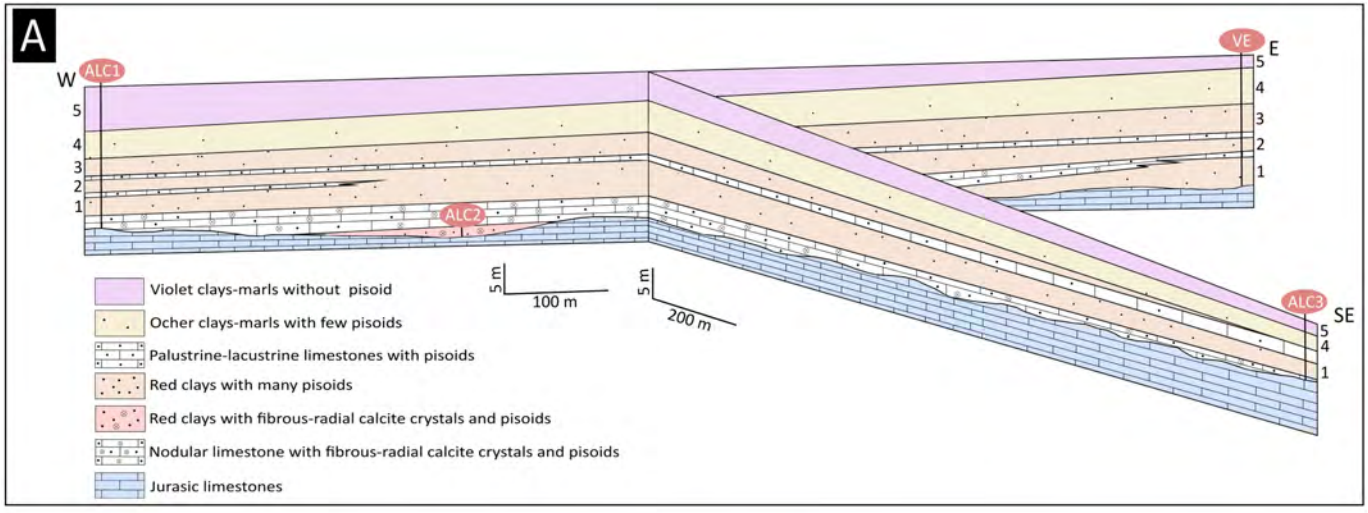
A
W
E
SE
ALC1
ALC2
ALC3
VE
5
4
3
2
1
5 m
100 m
5 m
200 m
Violet clays-marls without pisoid
Ocher clays-marls with few pisoids
Palustrine-lacustrine limestones with pisoids
Red clays with many pisoids
Red clays with fibrous-radial calcite crystals and pisoids
Nodular limestone with fibrous-radial calcite crystals and pisoids
Jurasic limestones


B
vc
oc
rc
LBS
UK

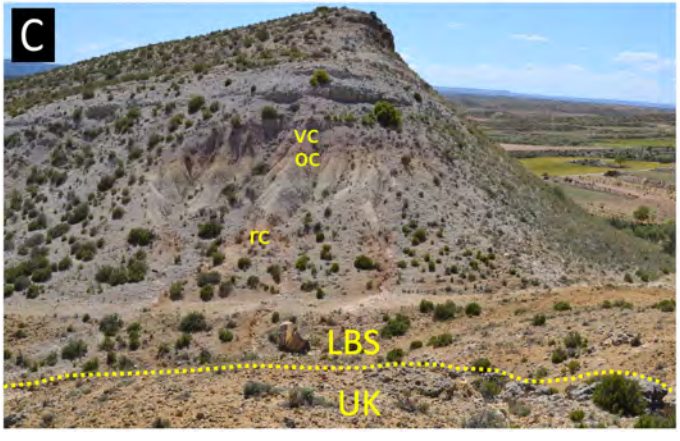
C
vc
oc
rc
LBS
UK

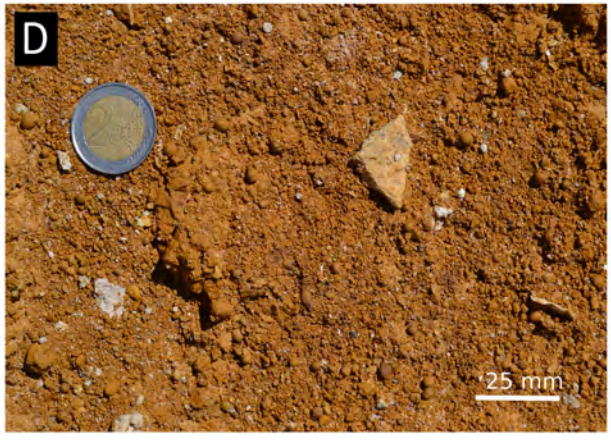
D
25 mm

Figure 3

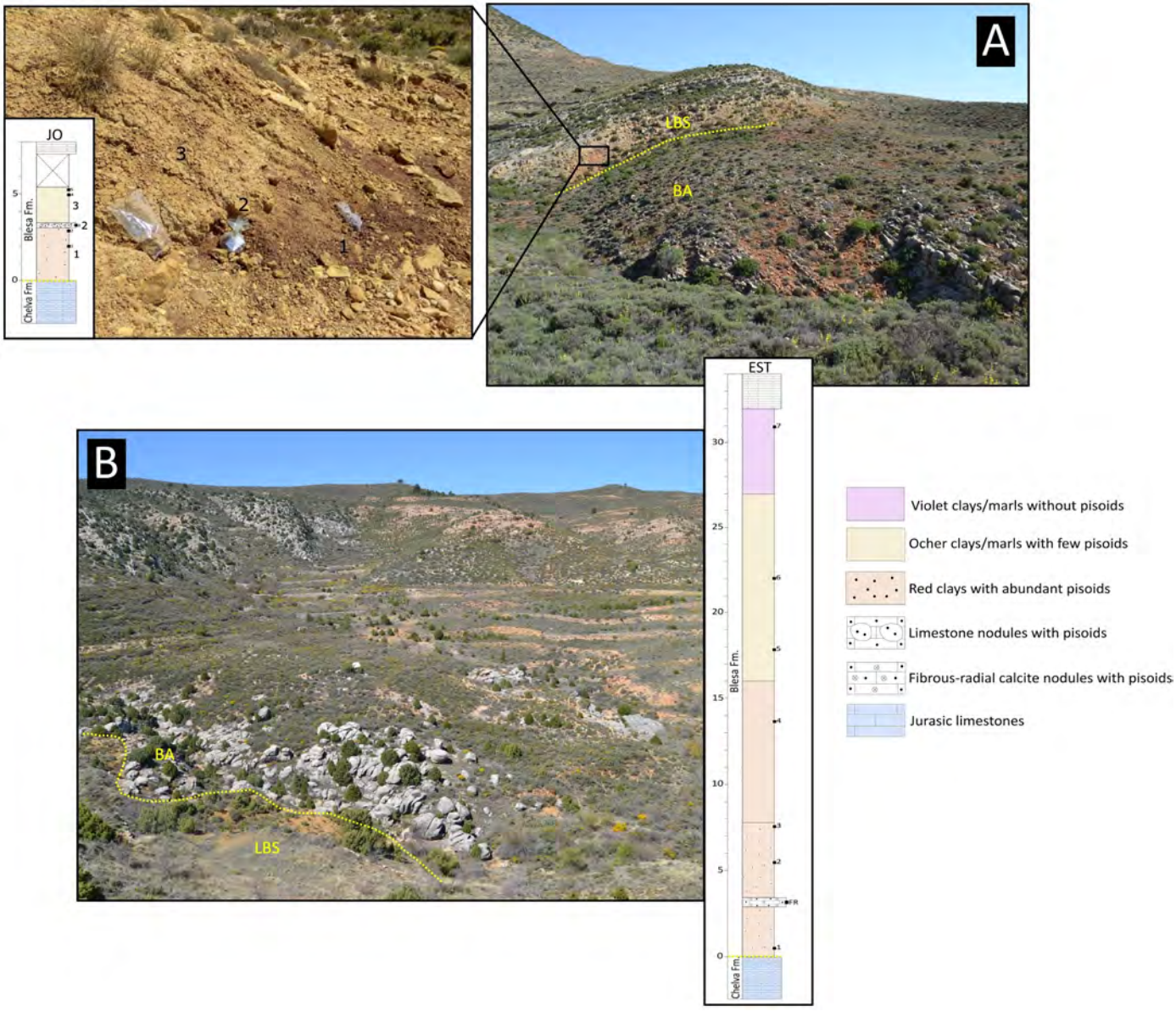
A
LBS
BA
JO
Blesa Fm.
Chelva Fm
3
2
1
B
BA
LBS
EST
Blesa Fm.
Chelva Fm
Violet clays/marls without pisoids
Ocher clays/marls with few pisoids
Red clays with abundant pisoids
Limestone nodules with pisoids
Fibrous-radial calcite nodules with pisoids
Jurasic limestones

Figure 4

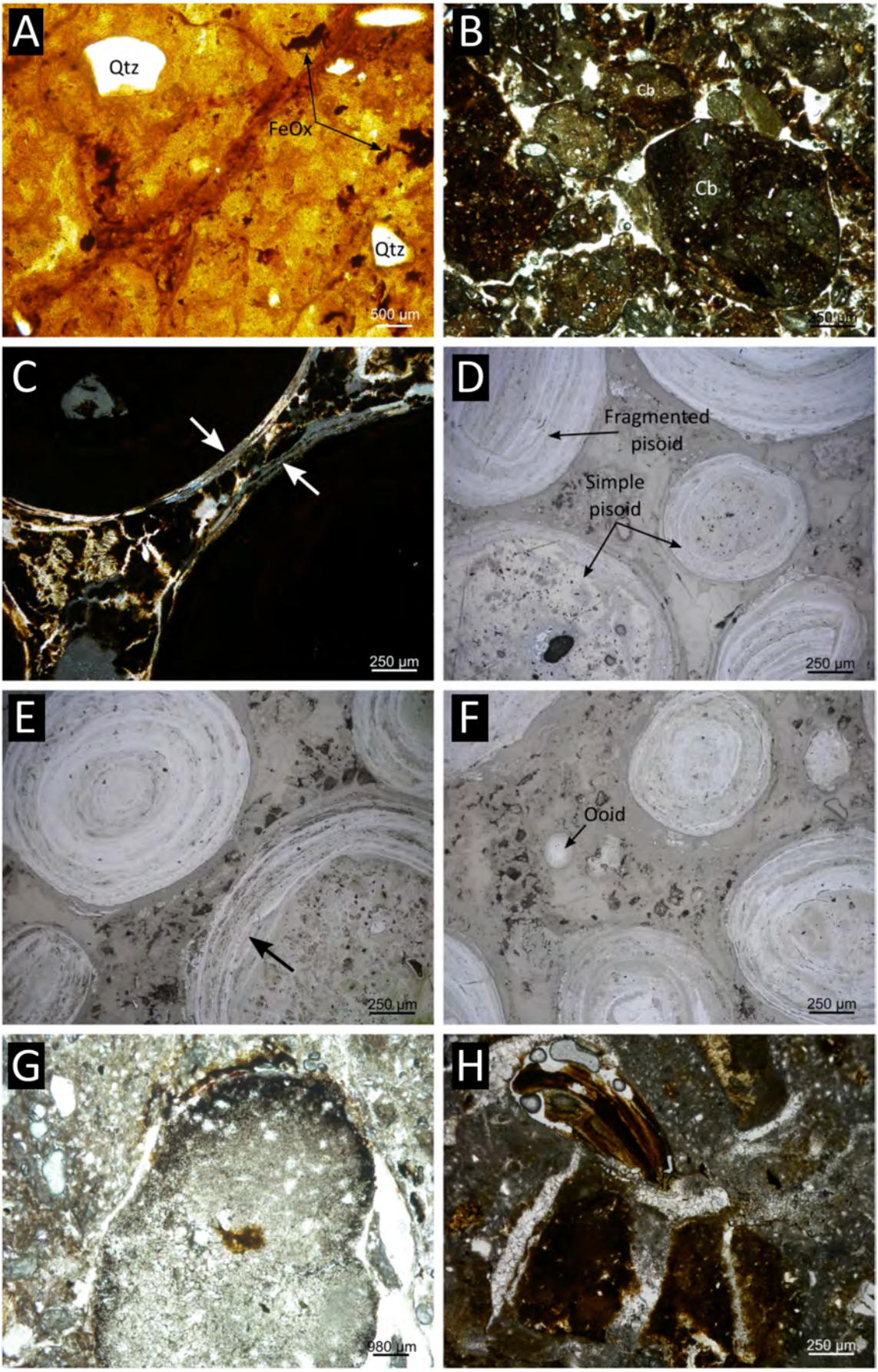
A
Qtz
FeOx
Qtz
500 µm
B
Cb
Cb
250 µm
C
250 µm
D
Fragmented pisoid
Simple pisoid
250 µm
E
250 µm
F
Ooid
250 µm
G
980 µm
H
250 µm

Figure 5

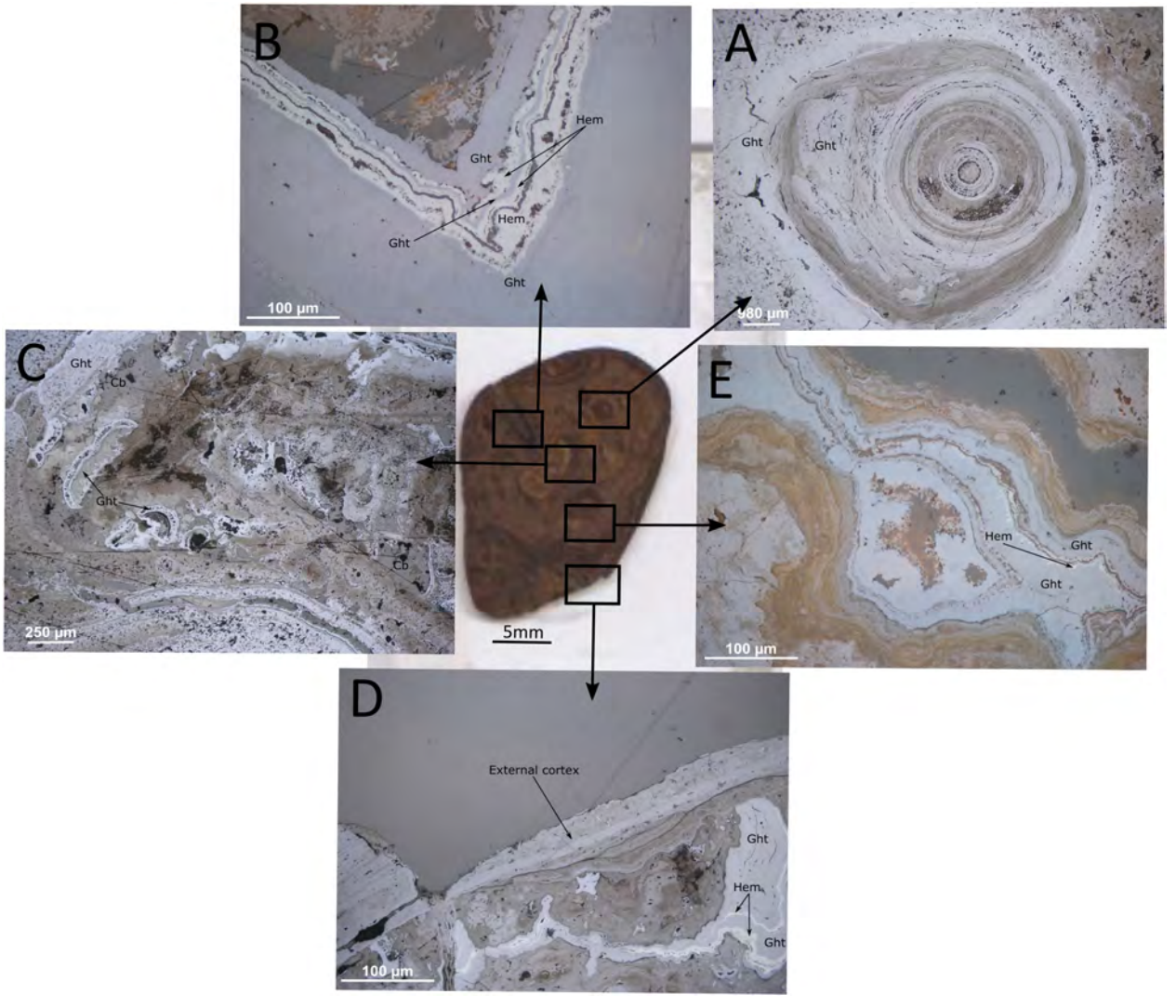
B
Hem
Ght
Hem
Ght
Ght
100 µm
A
Ght
Ght
80 µm
C
Ght
Cb
Ght
Cb
250 µm
5mm
E
Hem
Ght
Ght
100 µm
D
External cortex
Ght
Hem
Ght
100 µm

Figure 6

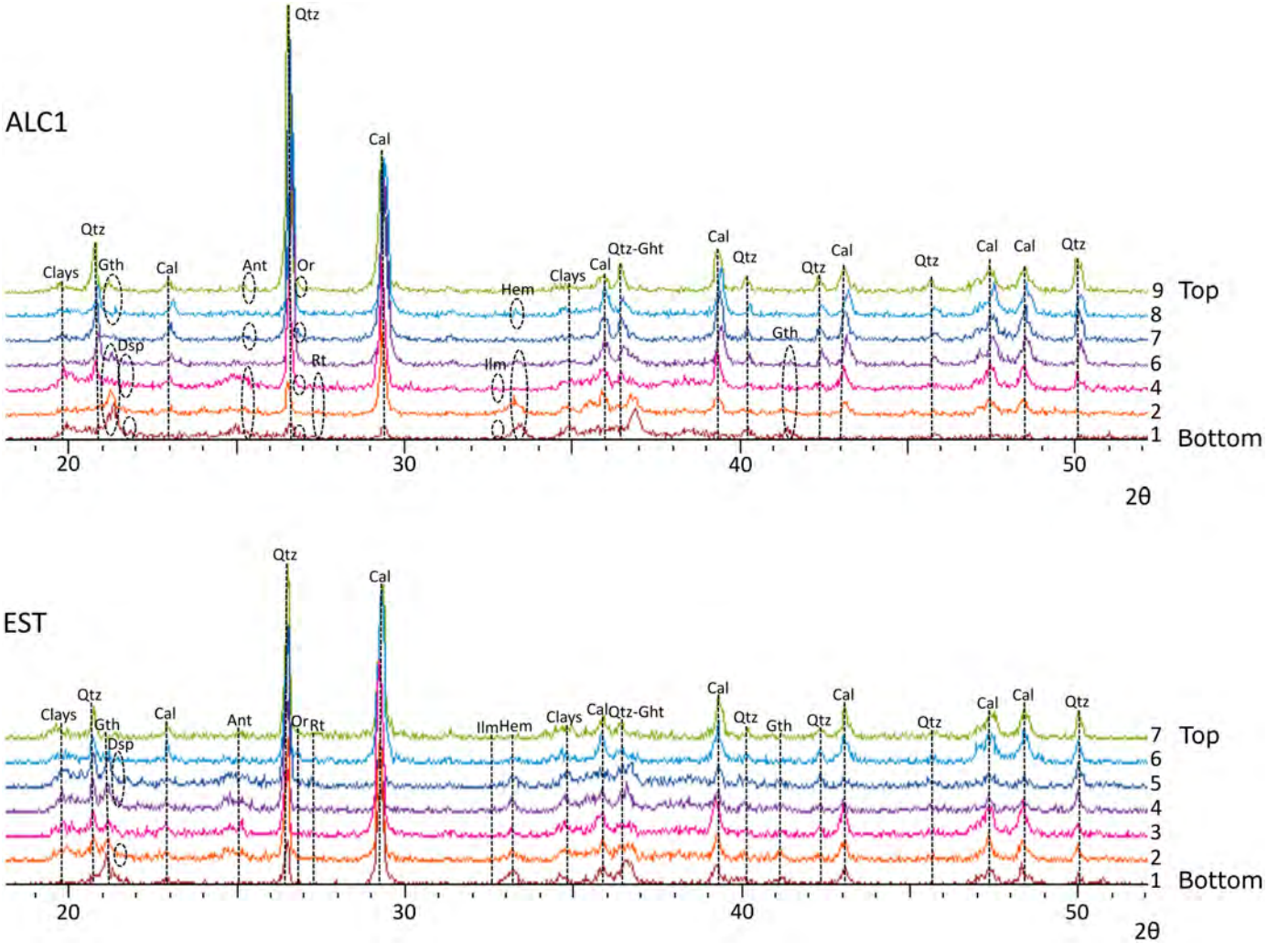
ALC1
Qtz
Cal
Clays
Gth
Dsp
Ant
Or
Rt
Hem
Ilm
Qtz-Ght
9
8
7
6
4
2
1
Top
Bottom
20
30
40
50
2θ
EST
Clays
Gth
Dsp
Ant
Or
Rt
Ilm
Hem
7
6
5
4
3
2
1
Top
Bottom
20
30
40
50
2θ

Figure 7

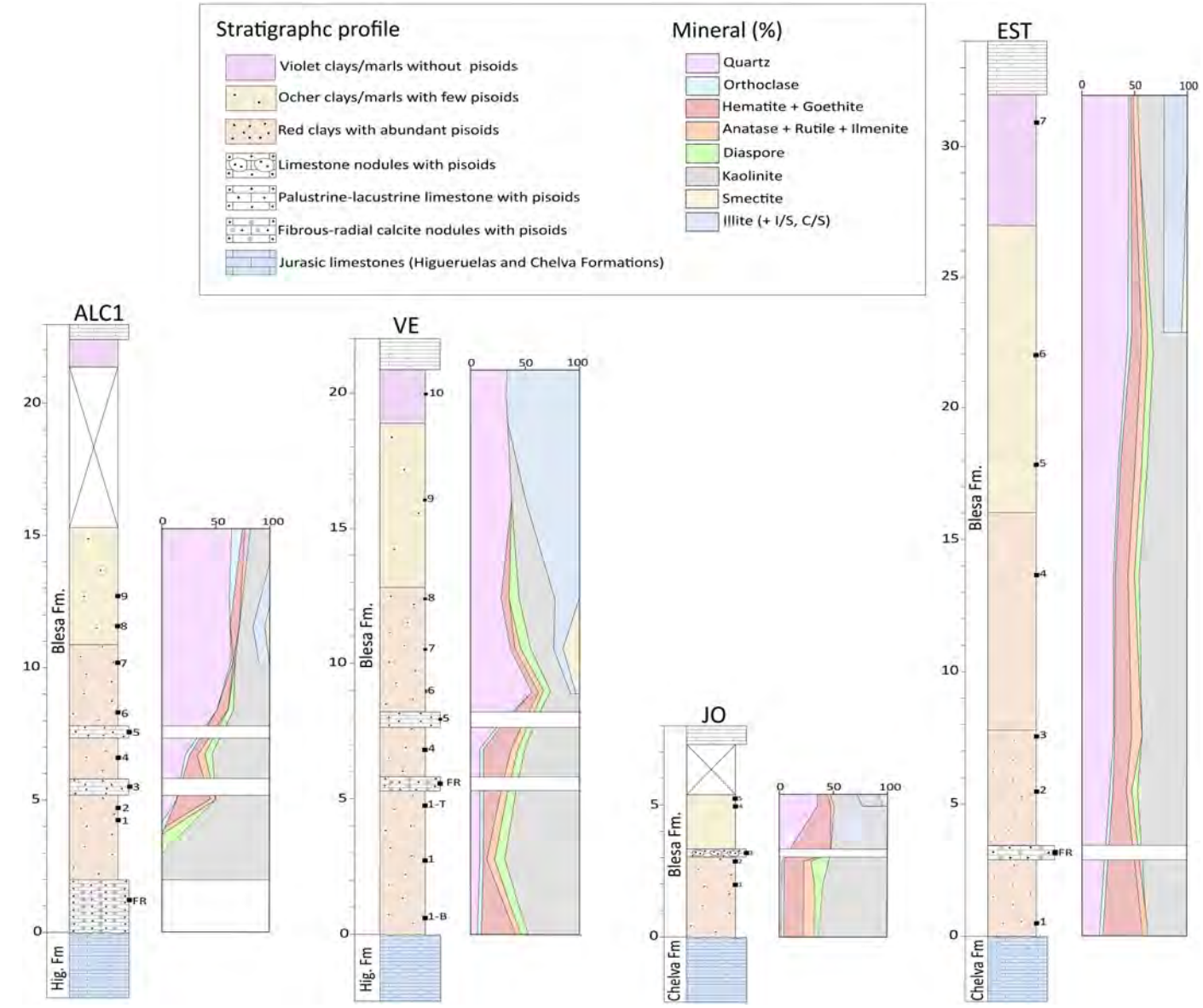
Stratigraphc profile
Violet clays/marls without pisoids
Ocher clays/marls with few pisoids
Red clays with abundant pisoids
Limestone nodules with pisoids
Palustrine-lacustrine limestone with pisoids
Fibrous-radial calcite nodules with pisoids
Jurasic limestones (Higueruelas and Chelva Formations)
Mineral (%)
Quartz
Orthoclase
Hematite + Goethite
Anatase + Rutile + Ilmenite
Diaspore
Kaolinite
Smectite
Illite (+ I/S, C/S)
ALC1
VE
JO
EST
Blesa Fm.
Hig. Fm
Chelva Fm
FR
0
50
100

Figure 8

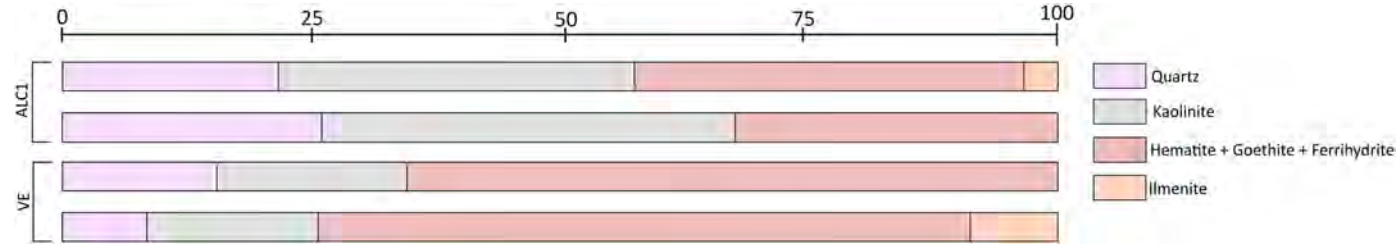
0
25
50
75
100
ALC1
VE
Quartz
Kaolinite
Hematite + Goethite + Ferrihydrite
Ilmenite

Figure 9

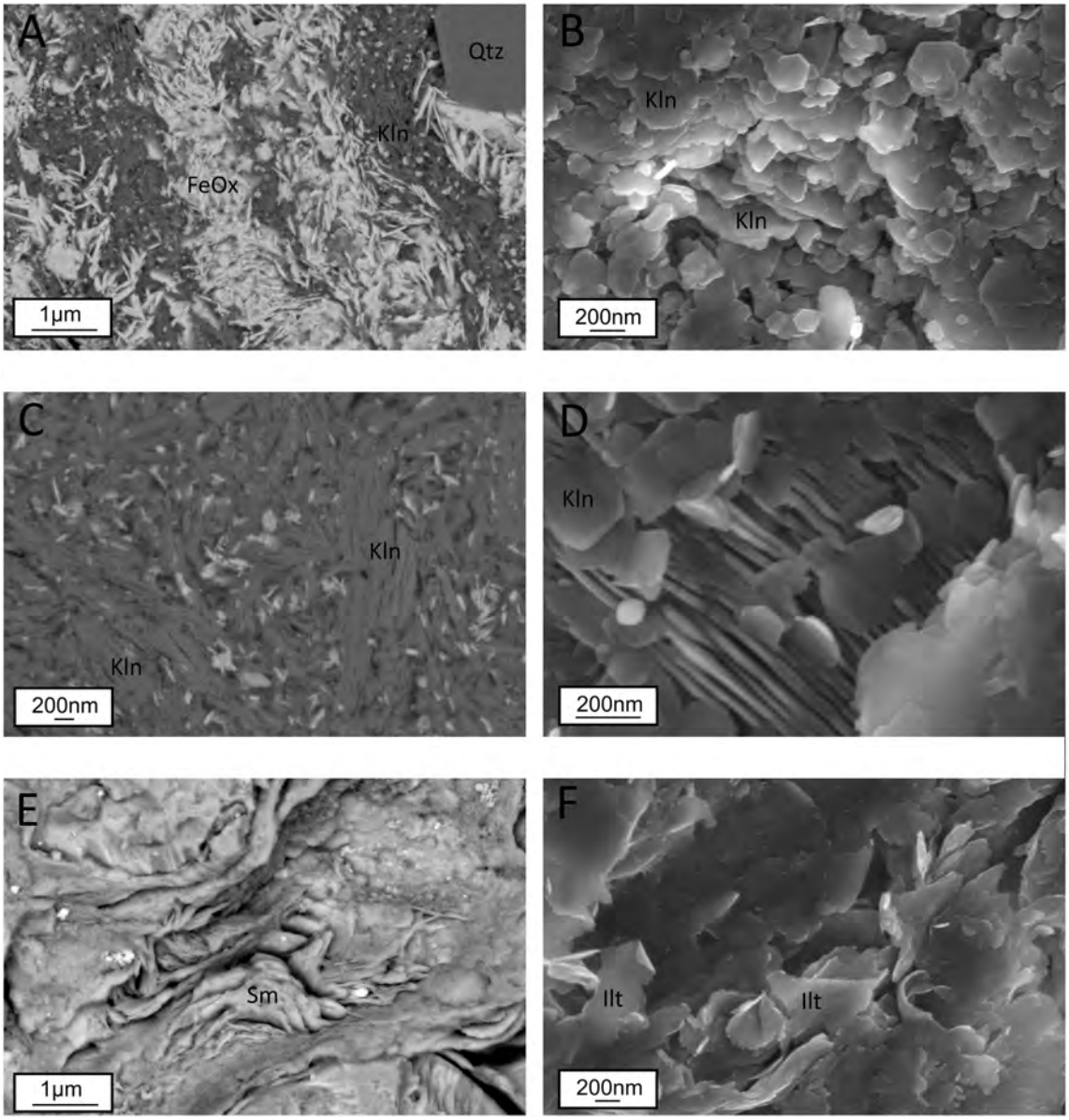
A
Qtz
Kln
FeOx
1µm
B
Kln
Kln
200nm
C
Kln
Kln
200nm
D
Kln
200nm
E
Sm
1µm
F
Ilt
Ilt
200nm

Figure 10

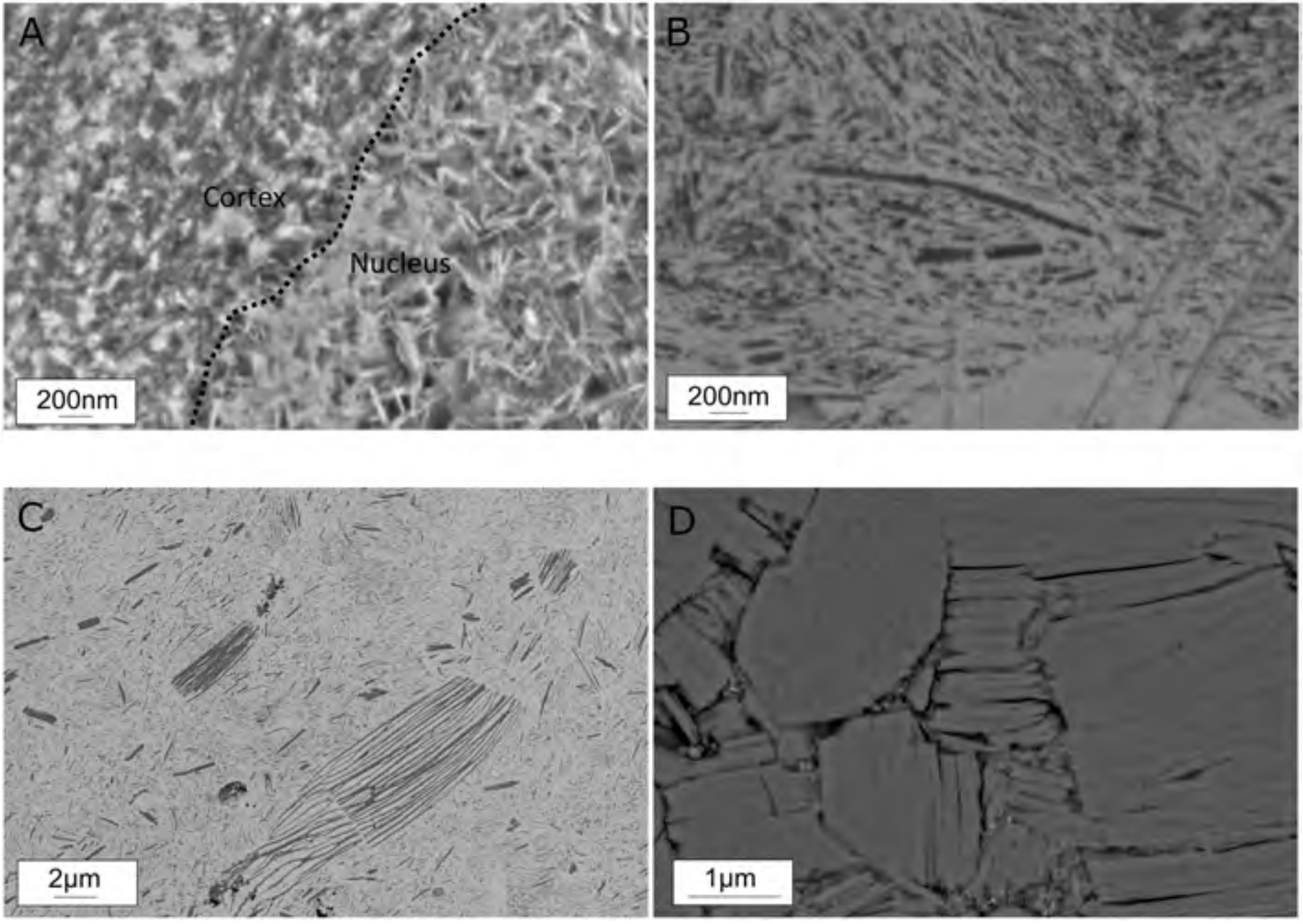

Figure 11

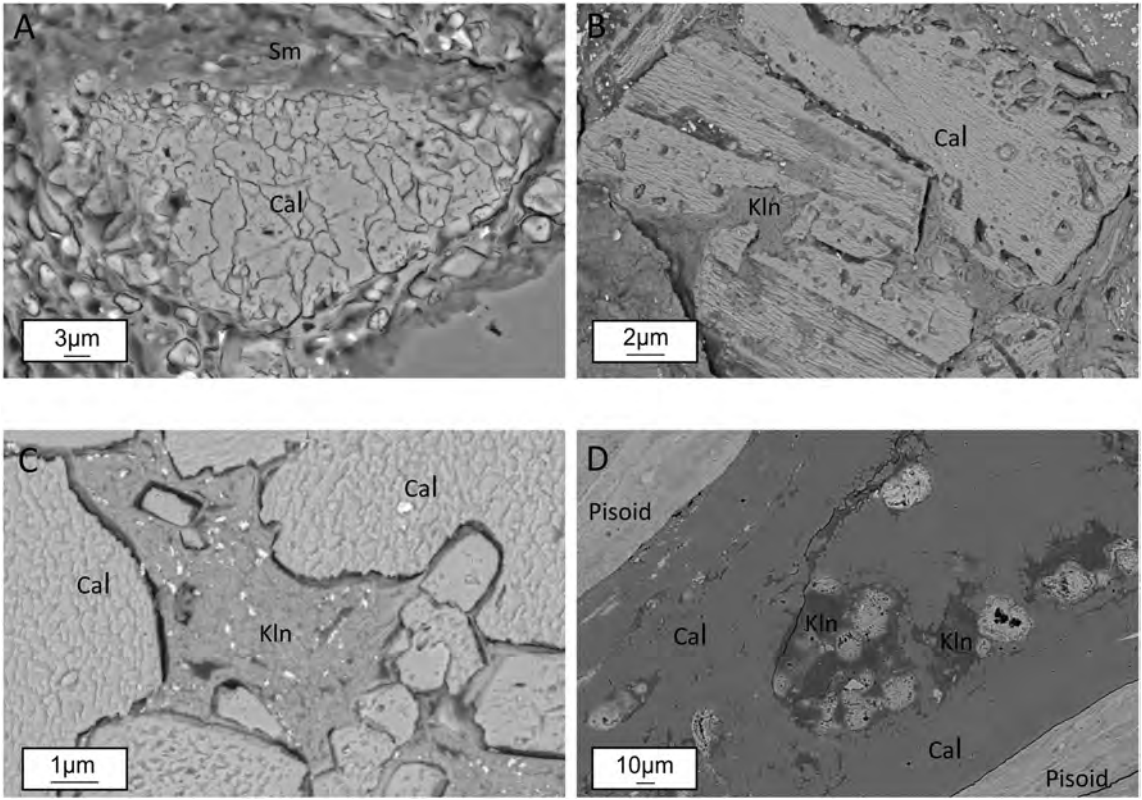
A
Sm
Cal
3µm
B
Cal
Kln
2µm
C
Cal
Cal
Kln
1µm
D
Pisoid
Cal
Kln
Kln
Cal
10µm
Pisoid

Figure 12